ARTICLES
PUBLISHED ONLINE: 19 JANUARY 2014 | DOI: 10.1038/NPHOTON.2013.350
nature photonics

White-light diffraction tomography of unlabelled live cells

Taewoo Kim[1†], Renjie Zhou[1,2†], Mustafa Mir[1], S. Derin Babacan[3], P. Scott Carney[4], Lynford L. Goddard[2] and Gabriel Popescu[1*]

We present a technique called white-light diffraction tomography (WDT) for imaging microscopic transparent objects such as live unlabelled cells. The approach extends diffraction tomography to white-light illumination and imaging rather than scattering plane measurements. Our experiments were performed using a conventional phase contrast microscope upgraded with a module to measure quantitative phase images. The axial dimension of the object was reconstructed by scanning the focus through the object and acquiring a stack of phase-resolved images. We reconstructed the three-dimensional structures of live, unlabelled, red blood cells and compared the results with confocal and scanning electron microscopy images. The 350 nm transverse and 900 nm axial resolution achieved reveals subcellular structures at high resolution in *Escherichia coli* cells. The results establish WDT as a means for measuring three-dimensional subcellular structures in a non-invasive and label-free manner.

A transparent object illuminated by an electromagnetic field generates a scattering pattern that carries specific information about its internal structure. Inferring this information from measurements of the scattered field, that is, solving the inverse scattering problem, is the fundamental principle that has allowed X-ray diffraction measurements to reveal the molecular-scale organization of crystals[1] and more recently, image cells with nanoscale resolution[2,3]. The scattered field is related to the spatially varying dielectric susceptibility of the scattering object by a transformation that simplifies considerably and, more importantly, becomes invertible, when the incident field is only weakly perturbed by the presence of the object. In this regime, the first-order Born approximation[4] and the Rytov approximation[5] have been used to unambiguously retrieve the three-dimensional spatial distribution of the dielectric constant. Implementation of inverse scattering requires knowledge of both the amplitude and phase of the scattered field. This obstacle, known as the phase problem, has been associated with X-ray diffraction measurement throughout its century-old history (for a review, see ref. 6).

In 1969, Wolf proposed diffraction tomography as a reconstruction method combining the X-ray diffraction principle with optical holography[7]. Unlike X-rays, light at lower frequencies can be used in phase imaging measurements, as demonstrated by Gabor[8]. In recent years, as a result of new advances in light sources, detector arrays and computing power, quantitative phase imaging (QPI), in which optical path-length delays are measured at each point in the field of view, has become a very active field of study[9]. Whether involving holographic or non-holographic methods[10–16], QPI presents new opportunities for studying cells and tissues non-invasively, quantitatively and without the need for staining or tagging[17–23]. Projection tomography using laser QPI has made use of ideas from X-ray imaging and enabled three-dimensional imaging of transparent structures[24–26]. More recently, this method has been applied to live cells[27–30]. This type of reconstruction has a complex set-up because of the requirement to either scan the illumination angle or rotate the specimen about a fixed axis. As a result, this method is limited to shallow depths of field[31]. Importantly, without additional efforts such as synthetic aperture[30] and digital de-noising techniques[32], laser light imaging is plagued by speckles, which ultimately limit the resolving power of the method[33]. To mitigate this problem, tomographic methods based on white light have also been proposed[34–36]. These approaches require *a priori* knowledge of the three-dimensional point spread function (PSF) of the instrument and ignore the physics of the light–specimen interaction. Despite these efforts, three-dimensional cell imaging is still largely restricted to confocal fluorescence microscopy, an invasive method[37].

Here, we report on a new approach for label-free tomography of live cells and other transparent specimens, which we refer to as white-light diffraction tomography (WDT). WDT offers a high-performance, simple design, as well as suitability for operation in a conventional microscopy setting. Its main features can be summarized as follows. First, WDT is a generalization of diffraction tomography to broadband illumination. Second, WDT operates in an imaging rather than a scattering geometry. Note that this is a departure from the far-zone, angular scattering that is traditionally used in X-ray diffraction. When dealing with transparent objects, measuring the complex field at the image plane yields higher sensitivity than measuring in the far-zone[38]. Third, WDT is implemented using an existing phase contrast microscope with white-light illumination, and the three-dimensional structure is recovered by simply translating the objective lens, which scans the focal plane axially through the specimen. Because phase contrast microscopes are commonly used, the method shown here could be adopted on a large scale by non-specialists.

[1]Quantitative Light Imaging Laboratory, Department of Electrical and Computer Engineering, Beckman Institute for Advanced Science and Technology, University of Illinois at Urbana-Champaign, Urbana, Illinois 61801, USA, [2]Photonic Systems Laboratory, Department of Electrical and Computer Engineering, Micro and Nanotechnology Laboratory, University of Illinois at Urbana-Champaign, Urbana, Illinois 61801, USA, [3]Beckman Institute for Advanced Science and Technology, University of Illinois at Urbana-Champaign, Urbana, Illinois 61801, USA, [4]Department of Electrical and Computer Engineering, Beckman Institute for Advanced Science and Technology, University of Illinois at Urbana-Champaign, Urbana, Illinois 61801, USA, †These authors contributed equally to this work. *e-mail: gpopescu@illinois.edu

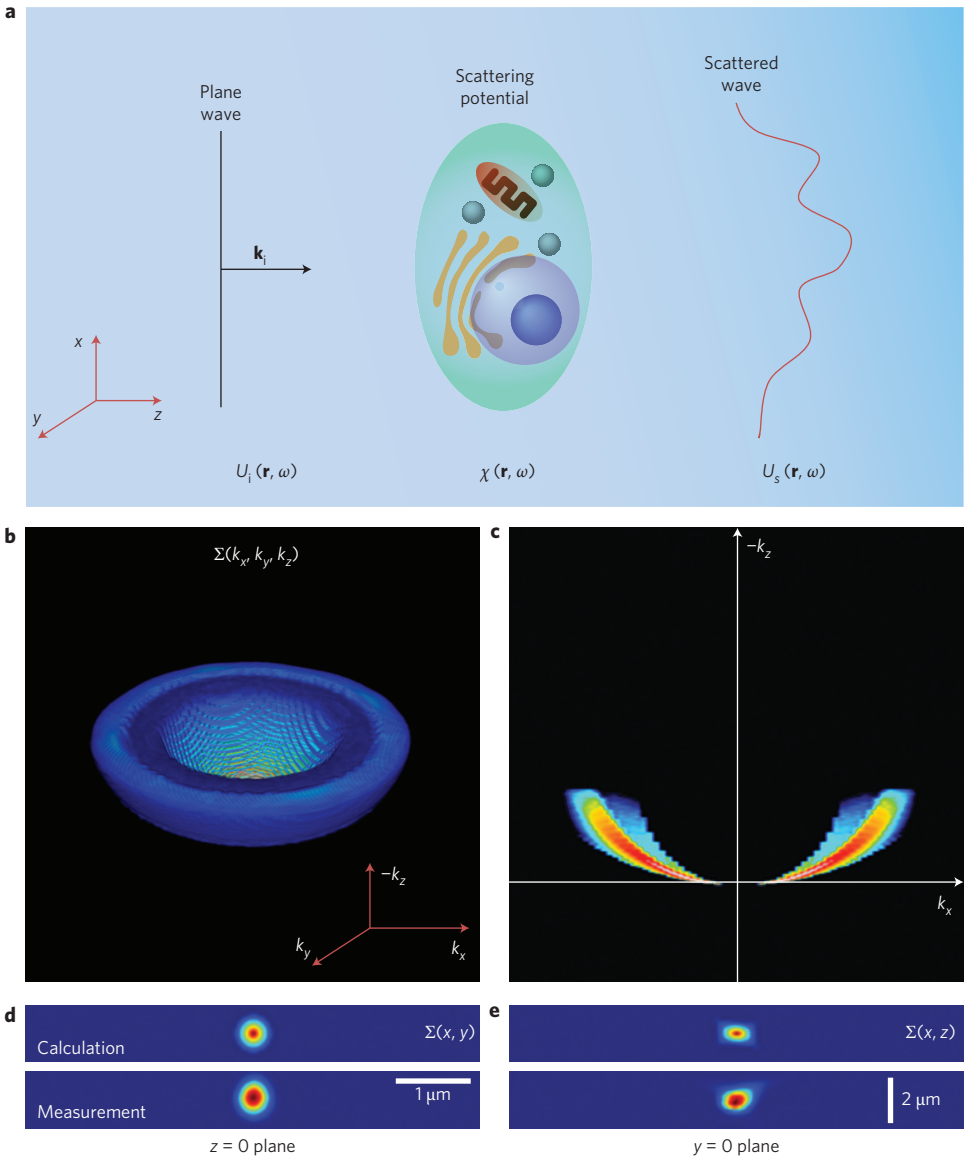

Figure 1 | The scattering problem. a, Illustration of light scattering under the first-order Born approximation where a plane wave's wavefront is perturbed by the object. **b**, Three-dimensional rendering of the instrument transfer function, using the proposed WDT calculation. **c**, Cross-section of the transfer function at the $k_y = 0$ plane. **d**, Calculated and measured PSF at the $z = 0$ plane. **e**, Calculated and measured PSF in the $y = 0$ plane.

Tomographic reconstruction and resolution

It is known that the Rytov approximation is more appropriate for reconstructing smooth objects with respect to the wavelength of light, that is, for low-resolution imaging, and the Born approximation works better for imaging finer structures (see, for example, ref. 39, p. 485). Accordingly, we use the latter here. Under the first-order Born approximation (Fig. 1a) with an incident plane wave $U_i = A(\omega)e^{i\beta(\omega)z}$, we solve the forward scattered field U_s in the wavevector space instead of using the traditional Green's function and Weyl's formula approach (see Methods and Supplementary Section b). In the transverse wavevector domain $\mathbf{k}_\perp$, U_s can be expressed as

$$U_s(\mathbf{k}_\perp, z; \omega) = -\frac{\beta_0^2(\omega)A(\omega)e^{iqz}}{2q}\chi[\mathbf{k}_\perp, q - \beta(\omega)] \qquad (1)$$

where $\beta(\omega) = \bar{n}\beta_0(\omega)$, with $\bar{n}$ being the spatial average of the refractive index associated with the object, $\beta_0(\omega) = \omega/c$ is the propagation constant (or the wavenumber) in vacuum, ω is the angular frequency, χ is the scattering potential of the non-dispersive object, $\chi(\mathbf{r}) = n^2(\mathbf{r}) - \bar{n}^2$ and $q = \sqrt{\beta^2(\omega) - k_\perp^2}$. (See Supplementary Section b and, for an alternative derivation[7].) The dispersion in the object is neglected, because most biological samples of interest here are weakly absorbing. This is true even for single red blood cells (RBCs). Even though haemoglobin absorbs strongly in blue, the overall absorption of visible light through a single RBC is very small. This is so because the absorption length of haemoglobin in a normal RBC is ~10 μm in the blue (averaged over wavelengths of 400–500 nm) and ~3 mm in the red (averaged over wavelengths of 600–750 nm)[40], while the thickness of the cell is only 2–3 μm. More discussion on the dispersion effect through a RBC is presented in the Supplementary Section i.

Note that, throughout this Article, we use the same symbol for a function and its Fourier transform. To indicate the domain in which the function operates, we carry all the arguments explicitly; for example, $f(\mathbf{k}_\perp, z; \omega)$ is the Fourier transform of $f(\mathbf{r}_\perp, z; t)$ over $\mathbf{r}_\perp$ and t. In conventional phase shifting interferometry, the cross-correlation of the scattered and reference fields is measured as

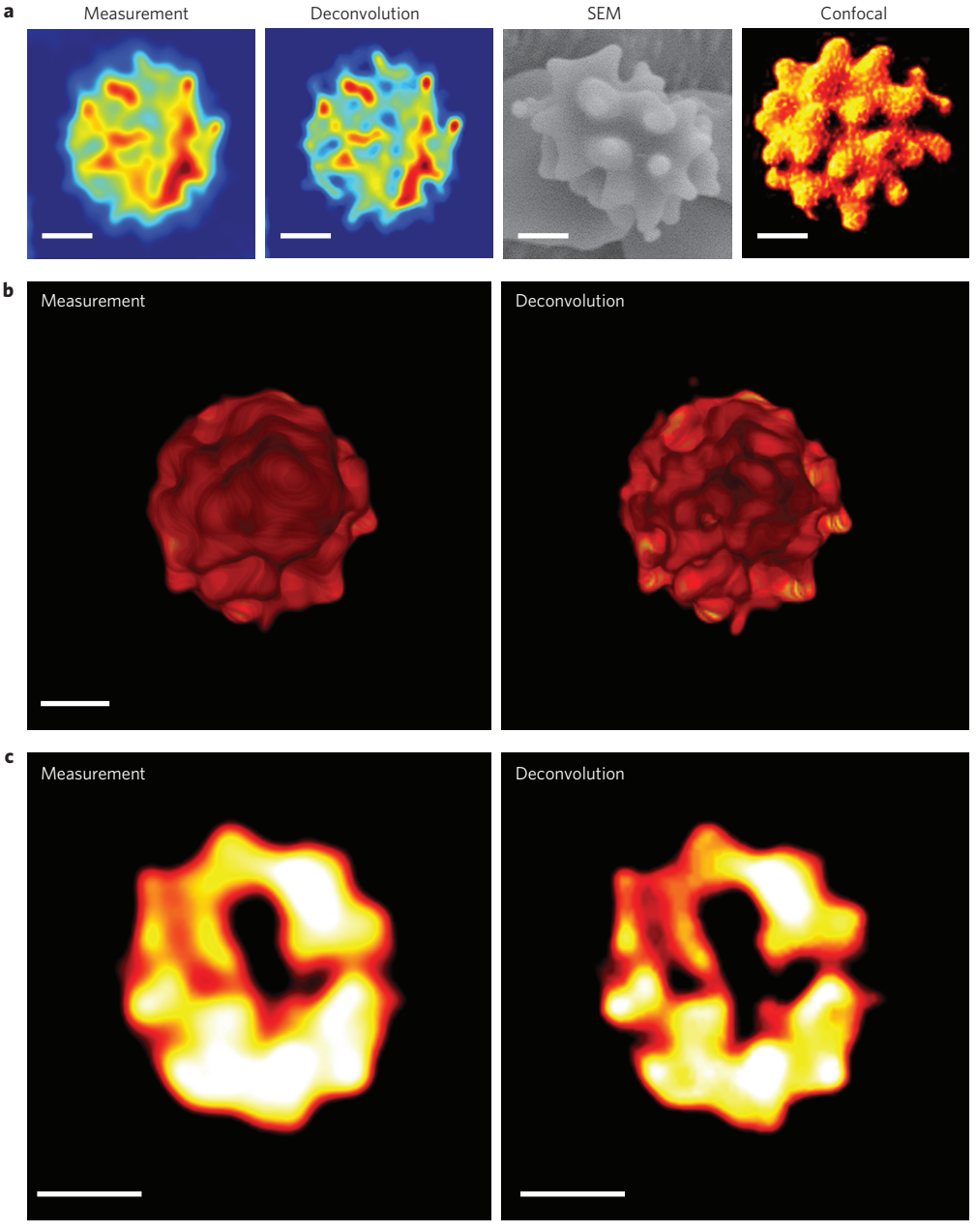

Figure 2 | WDT of RBCs. a, Measured *z*-slice of a spiculated RBC and the corresponding deconvolution using a ×40/0.75 NA objective. An SEM image and a confocal of similar cells are shown for comparison. **b**, Three-dimensional rendering of the raw data and the corresponding three-dimensional deconvolution (Supplementary Movie 1). **c**, A measured *z*-slice and the corresponding deconvolution result, showing the empty space between spicules on the RBC. Scale bars, 2 μm in space. The reconstruction uses a *z*-stack of 100 images, each with 128 × 128 pixels, which requires about 5 min for sparse deconvolution.

$\Gamma_{12}(\mathbf{r}_\perp, z, \tau) = \langle U_s(\mathbf{r}_\perp, z, t) U_r^*(z, t+\tau)\rangle$ at $\tau = 0$, which is equivalent to integrating the cross spectral density over ω. Knowledge of the spatial frequency response of our instrument, or coherent transfer function (see Supplementary Section c) $\Sigma(k_x, k_y, k_z)$, allows us to write the main result of our calculation (that is, the solution to the inverse scattering problem) in terms of the measured data Γ_{12} and the instrument function (or the coherent transfer function) Σ in the wavevector domain as

$$\chi(\mathbf{k}) = \frac{\Gamma_{12}(\mathbf{k}; 0)}{\Sigma(\mathbf{k})} \tag{2}$$

In practice, the operation in equation (2) requires regularization, as detailed in the Supplementary Section d. Transfer function $\Sigma(\mathbf{k})$ is given by

$$\Sigma(\mathbf{k}) = \frac{1}{8\bar{n}^2}\frac{\left(Q^2 + k_\perp^2\right)^2}{Q^3} S\left(-\frac{Q^2 + k_\perp^2}{2Q}\right) \tag{3}$$

where S is the optical spectrum of the imaging field as a function of the wavenumber and $Q = \sqrt{\beta^2 - k_\perp^2} - \beta$ (see Methods and Supplementary Section b). The three-dimensional PSF can be obtained through an inverse Fourier transform of equation (3).

Qualitatively, Σ has a physically intuitive behaviour (Fig. 1b–e). Specifically, its dependence on z is related to the optical spectrum $S(\omega)$ via a Fourier transform, meaning that a broader optical spectrum gives a narrower function, $\Sigma(z)$. This relationship explains the inherent optical sectioning capabilities of the instrument.

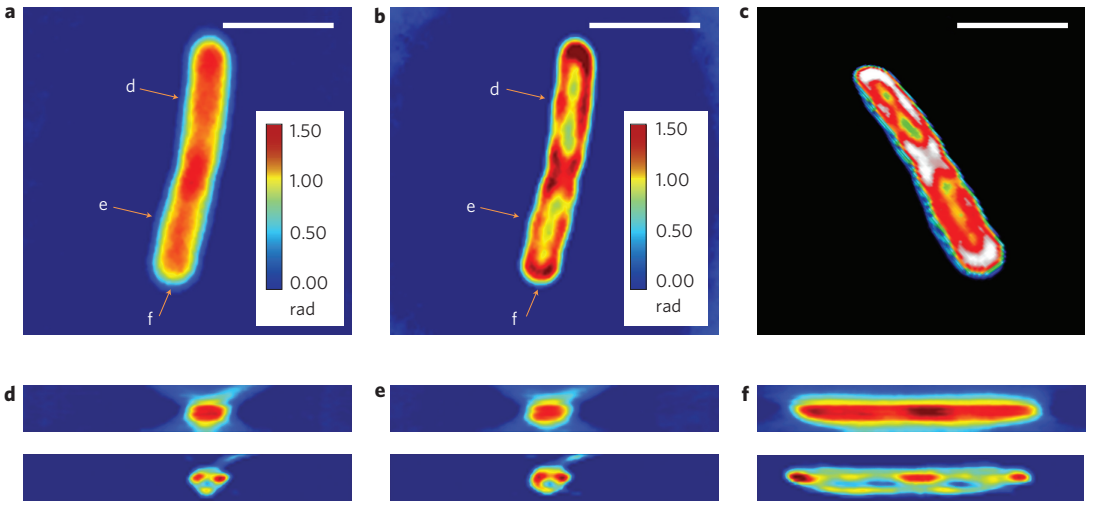

Figure 3 | WDT of *E. coli* cells. a, The centre frame of a *z*-stack measurement using a ×63/1.4 NA oil immersion objective. **b**, Deconvolution result of the same *z*-slice as in **a**, clearly showing a resolved helical structure. **c**, Centre cut of the three-dimensional rendering of the deconvolved *z*-stack, which shows both the overall cylindrical morphology and a helical subcellular structure (Supplementary Movie 2). **d**–**f**, Cross-sections of the measured *z*-stack (top row) and the deconvolved *z*-stack (bottom row). Each figure label corresponds to the markers shown in **a**,**b** and is in the same scale as **a**,**b**. Scale bars, 2 μm. A *z*-stack of 17 images, each with 128 × 128 pixels is used for the reconstruction, which requires about 3 min for sparse deconvolution.

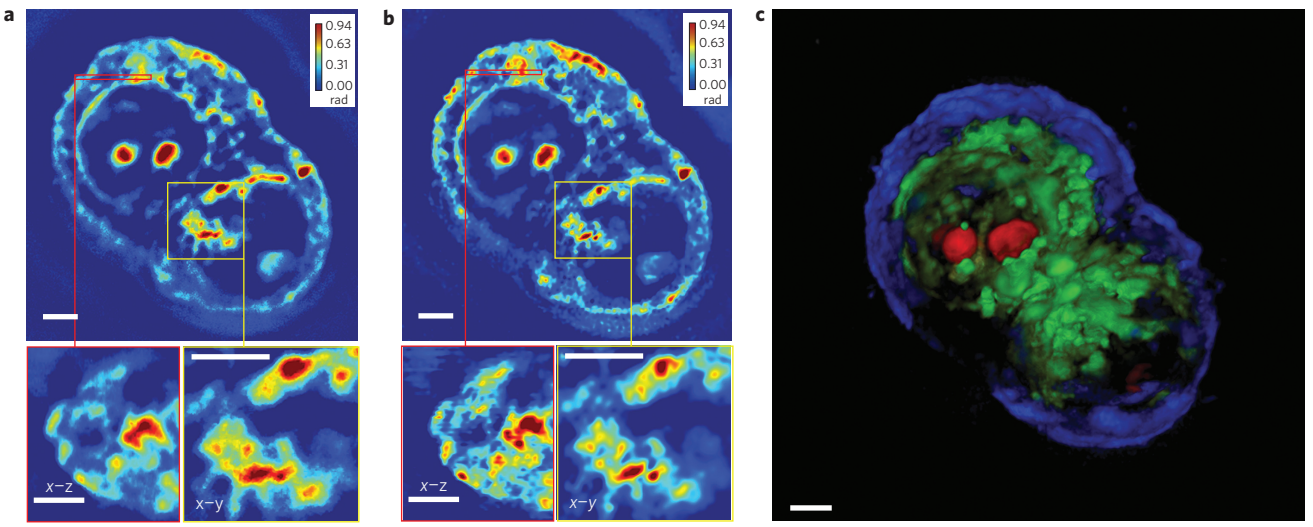

Figure 4 | WDT of HT29 cells. a, A measured *z*-slice (top), a cross-section at the area indicated by the red box (bottom left) and a zoomed-in image of the area indicated by the yellow box (bottom right), measured using a ×63/1.4 NA oil immersion objective. **b**, A deconvolved *z*-slice corresponding to the measurement shown in **a** (top), a cross-section at the area indicated by the red box (bottom left) and a zoomed-in image of the area indicated by the yellow box (bottom right). By comparing **a** and **b**, the resolution increase can be clearly seen. **c**, False-colour three-dimensional rendering of the deconvolution result (Supplementary Movie 3). We used *z*-stacks of 140 images, each with a dimension of 640 × 640. Owing to the large image dimension, the image is split into 25 sub-images for faster deconvolution. Overall, the deconvolution process took approximately an hour. Scale bars in all panels, 5 μm.

This type of optical gating, in which axial resolution is determined by the coherence properties of the illumination light, has been successfully applied in optical coherence tomography (OCT) of deep tissues[41,42]. However, there are significant differences between WDT and OCT. In OCT, the cross-correlation Γ_{12} is resolved over a broad delay range, which provides the depth dimension of the object. In WDT, the *z*-information is collected by scanning the focus through the object. Most importantly, in our method, the coherence gating works in synergy with the high-numerical-aperture (NA) optics and thus allows for high-resolution tomography. In other words, in WDT, coherence gating by itself would not work at zero NA and, conversely, high-NA gating would not work with monochromatic light.

We used broadband light from a halogen lamp and high-numerical-aperture objectives (×40/0.75 NA and ×63/1.4 NA), resulting in optical sectioning capabilities suitable for high-resolution tomography. Using high-NA objectives, polarization could play a role. However, for weakly scattering, isotropic objects, this effect is negligible. The function $\Sigma(k_x, k_y, k_z)$ for our imaging system is illustrated in Fig. 1b,c. As expected, the width of the k_z coverage increases with k_x, indicating that the sectioning is stronger for finer structures or, equivalently, higher scattering angles. The structure of the object is recovered through a sparse deconvolution algorithm (see Supplementary Section d). Figure 1d,e shows the transverse and longitudinal cross-sections of the calculated and measured $\Sigma(x, y, z)$, which determine the final resolution.

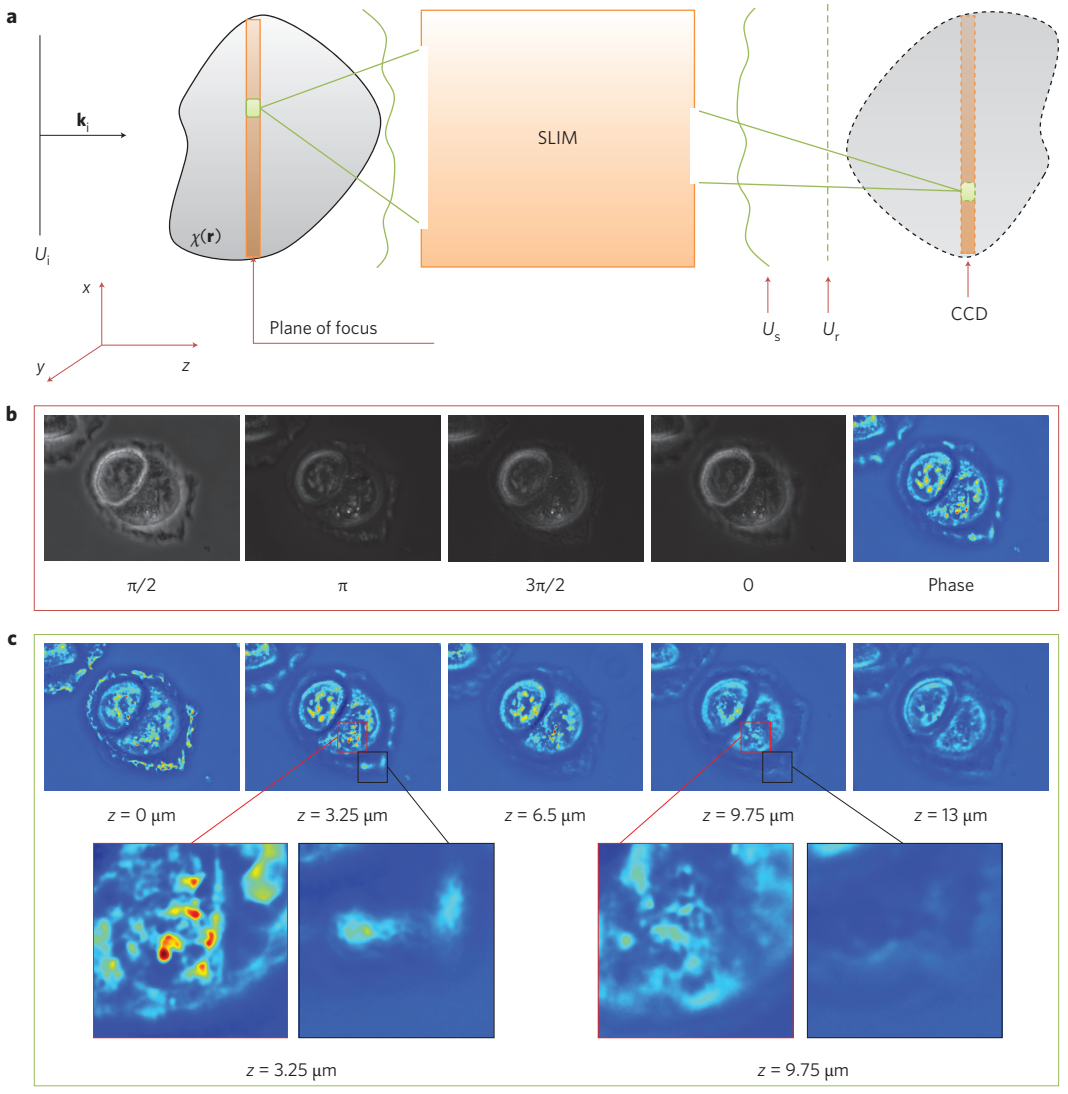

Figure 5 | Illustration of data acquisition. a, Optical sectioning in a phase contrast microscope, where an incident plane wave U_i is scattered by an object χ and the CCD measures the scattered field U_s and the reference field U_r. A detailed description of the SLIM model is provided in Supplementary Fig. 1. **b**, Example of phase reconstruction using four different phase-shifted intensity images. Applied phase shifts for each image are indicated. **c**, Example of optical sectioning in SLIM is shown as the focus scans through the U2OS cell over a range of 13 μm (top). Red and black outlined regions are zoomed in to more clearly show the optical sectioning ability (bottom). The colour scheme represents the phase value, with red representing large phase values and blue representing small phase values.

Experimentally, Σ was measured by imaging a microsphere much smaller than the resolution of the system, as detailed in the Supplementary Section d. The measured and experimental functions show good agreement, with the measured function being slightly larger than the calculations predict (0.39 μm versus 0.35 μm transversely; 1.22 μm versus 0.89 μm longitudinally). This is expected, as the particle used for the measurement has a finite thickness that adds to the width of Σ.

Tomography of spiculated RBCs

After validating our WDT method using a polystyrene microbead sample (see Supplementary Section h), we first applied WDT to measure spiculated RBCs, known as echinocytes. This morphological abnormality is well documented and can be an indication of transitory stress (for example, osmotic stress) or a sign of a serious disease[21,43]. We used this interesting three-dimensional morphology as a test sample and used a scanning electron microscopy (SEM) image and a confocal fluorescence microscopy image[44] as control imaging methods (Fig. 2a) . The sample was prepared as a blood smear on a glass slide, and phase images were measured using spatial light interference microscopy (SLIM), as described in the Methods. Unlike SEM and confocal microscopy, which require sample preparation steps such as metal deposition and fluorescence labelling (Calcein and DiI in Fig. 2a), WDT is label-free and works without sample preparation. Furthermore, the irradiance at the sample plane in WDT is six to seven orders of magnitude lower than in confocal microscopy[16], which provides a less harmful environment for the sample. Axial data (z-stack) were acquired in steps of 250 nm and a precision of 10 nm was ensured by the piezoelectric nosepiece. With the $\Sigma(x, y, z)$ function computed for a ×40/0.75 NA objective, we performed the three-dimensional deconvolution based on the sparsity constraint[34,45] (see Supplementary Section d). Figure 2a presents a SLIM projection image of an echinocyte and its corresponding deconvolved image, as well as an SEM image of a similar echinocyte. Sharper surface structures are observed for the RBC in the deconvolved image, as expected. Figure 2b shows the three-dimensional rendering of the raw z-stack images, as well as the corresponding deconvolution, as

indicated (Supplementary Movie 1). Again, the protrusions in the cell membrane show more details in the deconvolved image. This result is more clearly demonstrated by investigating one slice from the tomogram, as shown in Fig. 2c, in which the empty space between spicules is revealed in greater detail after deconvolution.

Tomography of *Escherichia coli*

We further applied our approach to image *E. coli* cells. We acquired a *z*-stack consisting of 17 slices with a step size of 280 nm. Figure 3a,b shows the middle frame of raw data and the reconstructed *z*-stack. Upon deconvolution, the previously invisible protein helical subcellular structure of *E. coli* is resolved. These interesting structures have recently been investigated as a result of the development of high-resolution fluorescence microscopy techniques, with which the subcellular localizations of different proteins, such as the MinCD complex, FtsZ and MreB, are recorded. It has also been discovered that this helical structure is also related to lipopolysaccharides deposition[34,46–48]. The three-dimensional rendering of this *E. coli* cell is shown in Fig. 3c. Only the bottom half of the cell is shown in the figure to emphasize the helical subcellular structure (Supplementary Movie 2). Figure 3d–f presents profiles along the lines indicated in Fig. 3a–c.

Tomography of HT29 cells

To study more complex subcellular structures, we imaged human colon adenocarcinoma cells (HT29), using a ×63/1.4 NA oil immersion objective. The *z*-stack, consisting of 140 frames, was acquired in 150 nm *z*-steps. More details on the deconvolution algorithm are presented in the Supplementary Section d. The results obtained on a cell that has recently divided are summarized in Fig. 4. At the bottom of Fig. 4a,b we show specific regions of interest in *x*–*z* and *x*–*y* cross-sections. An increase in resolution is apparent in both the longitudinal (left, red box) and transverse (right, yellow box) directions. We used the deconvolved *z*-stack to generate the three-dimensional rendering of the HT-29 cell. WDT, like other quantitative phase imaging techniques, does not provide specificity, so subcellular structures are selected using a combination of features, including shape and refractive index. For example, nucleoli have the highest refractive indices in the cell and the nuclear membrane surrounding them typically reveals the cell nuclei. Figure 4c (Supplementary Movie 3) presents a false-colour three-dimensional image of an HT-29 cell, in which we can clearly observe the subcellular structures (cell membrane in blue; nuclei in green; nucleoli in red). These areas are first chosen by thresholding based on the phase values (0.6 rad for nucleoli; 0.1 rad for membrane) and then detailed based on morphology.

Summary and discussion

Our study shows that using spatially coherent and temporally incoherent light, three-dimensional structure information can be retrieved unambiguously, simply by scanning the focus through the object of microscope. This type of reconstruction requires a new theoretical description of the interaction between a weakly scattering object and broadband light, which we present here for the first time. In essence, our theory generalizes Wolf's diffraction tomography[7] to white light and correctly predicts that the sectioning capability is the result of the combined effect of coherence and high-NA gating. As a result, we can calculate the imaging system's response (PSF) and quantify the resolution, which turns out to be 350 nm transversally and 890 nm axially. Solving scattering problems using a quantitative phase microscope—that is, measuring at the image plane instead of the far-zone—is a powerful new concept that allows us to acquire light scattering data from completely transparent objects with high sensitivity and dynamic range. In practical terms, WDT renders three-dimensional images of unlabelled cells in the traditional environment of an inverted microscope, allowing for cell imaging over an extended period of time. Indeed, in the Supplementary Section g, we show HeLa cell three-dimensional imaging with WDT over a period of 24 h. Accordingly, we anticipate that WDT will become a standard imaging modality in cell biology, complementing established technologies such as confocal microscopy.

Methods

Imaging. The specimen of interest was imaged with an inverted phase contrast microscope (Zeiss Axio Observer Z1) and white-light illumination. At the camera port, the microscope is equipped with a SLIM module, which renders quantitative phase images with subnanometre path-length sensitivity both spatially and temporally (see ref. 16 for details). To measure the axial dimension, the focal plane is scanned through the object by axially translating the objective lens (Fig. 5a). At each *z*-position of the object, a charge-coupled device (CCD) records the interferogram between the scattered (U_s) and unscattered (U_r) fields. For a more detailed description of the SLIM module, see Supplementary Fig. 1. The SLIM module introduces controllable phase shifts to U_r in increments of $\pi/2$ such that a unique quantitative phase image is reconstructed from four intensity images, as shown in Fig. 5b and detailed in the Supplementary Section a. This acquisition process is repeated with an acquisition speed of 8 frames per second (f.p.s.), which translates to two quantitative images per second as the focus is scanned through the object by moving the objective lens, and the entire SLIM image *z*-stack is saved to disk for further processing. This acquisition speed is limited only by the detector frame rate and the refresh rate of the spatial light modulator. In the Supplementary Information we describe in detail the computer synchronization of data acquisition, as well as axial sampling and accuracy. Furthermore, we have previously demonstrated that SLIM can be used in parallel with other microscope imaging modalities such as fluorescence imaging, differential interference contrast, or bright-field[16,22]. Therefore, combining these modalities with WDT can also be done in order to obtain three-dimensional high-resolution quantitative phase images with specificity. Because of its low exposure and phototoxicity, SLIM is capable of measuring over an extended period of time. Note that the environmental control is a standard accessory for the existing commercial microscope base. Accordingly, WDT can be used for four-dimensional imaging, with the fourth dimension being time. We provide more details on this capability in the Supplementary Section g.

It is clear from the raw *z*-stack data (Fig. 5c) that optical sectioning is present in our quantitative phase images. However, to translate this phase information, which is a property of the optical field, into tomographic information, describing the object itself, we must develop a new inverse scattering theory to describe the white light–object interaction. In essence, we extended the diffraction tomography calculations to white-light illumination and expressed the result in terms of the field cross-correlation function, which is the measurable quantity. In the following, we provide the main steps in our derivation (a detailed derivation is provided in the Supplementary Section b).

Theory. As discussed in the Supplementary Section a, the measurable quantity in our phase shifting experiments is the temporal cross-correlation function Γ_{12} between the scattered field U_s and the reference plane wave field U_r evaluated at the origin, that is, around the zero delay or $\tau = 0$. Γ_{12} is defined as

$$\Gamma_{12}(\mathbf{r}, \tau) = \langle U_s(\mathbf{r}, t) U_r^*(\mathbf{r}, t+\tau) \rangle \tag{4}$$

where the asterisk denotes complex conjugation and the angle brackets denote ensemble averaging. The generalized Wiener–Khintchine theorem[49,50] allows us to relate Γ_{12} to the cross-spectral density, $W_{12}(\mathbf{r}, \omega) = \langle U_s(\mathbf{r}, \omega) U_r^*(\mathbf{r}, \omega) \rangle$, via a simple Fourier transform. Therefore, the measured cross-correlation at zero time delay can be expressed as an integral of the cross spectral density over all angular frequencies:

$$\begin{aligned} \Gamma_{12}(\mathbf{r}, \tau = 0) &= \int_0^\infty W_{12}(\mathbf{r}, \omega) e^{-i\omega\tau} \mathrm{d}\omega \\ &= \int_0^\infty \langle U_s(\mathbf{r}, \omega) U_r^*(\mathbf{r}, \omega) \rangle \mathrm{d}\omega \end{aligned} \tag{5}$$

To calculate the integral in equation (5), we first derive a solution for the scattered field, U_s. The general scattering problem can be formulated by considering Fig. 1a. The Helmholtz equation, which describes the total field U, is given as

$$\nabla^2 U(\mathbf{r}, \omega) + \beta^2(\omega) U(\mathbf{r}, \omega) = -\chi(\mathbf{r}) \beta_0^2(\omega) U(\mathbf{r}, \omega) \tag{6}$$

where $\beta(\omega) = \bar{n}\beta_0(\omega)$, with $\bar{n}$ being the spatial average of the refractive index associated with the object ($\bar{n} = \langle n(\mathbf{r}) \rangle_r$), which is assumed to be non-dispersive, $\beta_0(\omega) = \omega/c$ is the propagation constant (or the wavenumber) in vacuum, ω is the

angular frequency, χ is the scattering potential of the non-dispersive object ($\chi(\mathbf{r}) = n^2(\mathbf{r}) - \bar{n}^2$), and n is the inhomogeneous refractive index associated with the object. U can be written as the summation of the incident and scattered field, $U(\mathbf{r},\omega) = U_i(\mathbf{r},\omega) + U_s(\mathbf{r},\omega)$, where $U(\mathbf{r},\omega) = A(\omega)e^{i\beta(\omega)z}$ is the incident wave ($A(\omega)$ is the spectral amplitude of the incident field) and U_s is the scattered wave, which is described by the reduced wave equation,

$$\nabla^2 U_s(\mathbf{r},\omega) + \beta^2(\omega)U_s(\mathbf{r},\omega) = -\chi(\mathbf{r})\beta_0^2(\omega)U(\mathbf{r},\omega) \tag{7}$$

The right-hand side of equation (7) is due to the scattering from the object, which acts as a secondary light source. We use the first-order Born approximation (see, for example, section 13.1.2. in ref. 4), which considers the scattering to be so weak, $|U_s(\mathbf{r},\omega)| << |U_i(\mathbf{r},\omega)|$, that the field inside the object remains essentially a plane wave. This is a reasonable approximation in the context of imaging cells. Under these circumstances, on the right-hand side of equation (7) we can replace U with $U_i(\mathbf{r},\omega) = A(\omega)e^{i\beta(\omega)z}$. Instead of using the traditional Green's function approach and Weyl's formula[7], we solve this equation in the wavevector space (see chapter 2 in ref. 9). Thus, Fourier-transforming equation (7) with respect to $\mathbf{r}$ (see Supplementary Section b), we obtain the solution for the scattered field in the $\mathbf{k}$-domain,

$$U_s(\mathbf{k},\omega) = -\beta_0^2(\omega)A(\omega)\frac{\chi[\mathbf{k}_\perp, k_z - \beta(\omega)]}{q^2(\mathbf{k}_\perp,\omega) - k_z^2} \tag{8}$$

In equation (8), $\mathbf{k} = (k_x, k_y, k_z)$ is the wavevector, $\mathbf{k}_\perp = (k_x, k_y)$ is the transverse wavevector, and $q(\mathbf{k}_\perp,\omega) = \sqrt{\beta^2(\omega) - k_\perp^2}$. The denominator in equation (8) can be decomposed into two terms, $1/[k_z - q(\omega)]$ and $1/[k_z + q(\omega)]$, which correspond to the forward-scattering and back-scattering terms, respectively. Because our experiments are performed in transmission and we only measure forward-scattering waves, we retain the former term. We now take the inverse Fourier transform of equation (8) with respect to k_z. We therefore obtain the forward scattering field as a function of transverse wavevector $\mathbf{k}_\perp$, axial distance z and angular frequency ω:

$$U_s(\mathbf{k}_\perp, z;\omega) = -\frac{\beta_0^2(\omega)A(\omega)e^{iqz}}{2q}\chi[\mathbf{k}_\perp, q - \beta(\omega)] \tag{9}$$

Using the solution for U_s from equation (9), we perform the integral in equation (5), which, after straightforward manipulations and change of variables (see Supplementary Section b), gives the following simple expression for the measured signal versus the transverse wavevector and axial distance,

$$\Gamma_{12}(\mathbf{k}_\perp, z; 0) = \Sigma(\mathbf{k}_\perp, z) \circledcirc_z \chi(\mathbf{k}_\perp, -z) \tag{10}$$

where $\circledcirc_z$ represents a convolution operation along the axial dimension z, between the object scattering potential χ and the instrument function Σ. More explicitly, the instrument function can be expressed as

$$\Sigma(\mathbf{k}_\perp, z) = \frac{1}{8\bar{n}^2} FT_Q^{-1}\left[\frac{(Q^2 + k_\perp^2)^2}{Q^3} S\left(-\frac{Q^2 + k_\perp^2}{2Q}\right)\right]_z \tag{11}$$

Importantly, our theory uses no approximations on propagation (for example, no Fraunhoffer, or even Fresnel, approximations are used), which makes it suitable for high-resolution imaging.

Received 26 February 2013; accepted 26 November 2013; published online 19 January 2014

References

1. Als-Nielsen, J. & McMorrow, D. *Elements of Modern X-ray Physics* (Wiley, 2001).
2. Jiang, H. *et al.* Quantitative 3D imaging of whole, unstained cells by using X-ray diffraction microscopy. *Proc. Natl Acad. Sci. USA* **107,** 11234–11239 (2010).
3. Raines, K. S. *et al.* Three-dimensional structure determination from a single view. *Nature* **463,** 214–217 (2010).
4. Born, M. & Wolf, E. *Principles of Optics: Electromagnetic Theory of Propagation, Interference and Diffraction of Light* 7th expanded edn (Cambridge Univ. Press, 1999).
5. Devaney, A. J. Inverse-scattering theory within the Rytov approximation. *Opt. Lett.* **6,** 374–376 (1981).
6. Wolf, E. in *Advances in Imaging and Electron Physics* Vol. 165 (ed. Hawkes, P. W.) Ch. 7 (Academic, 2011).
7. Wolf, E. Three-dimensional structure determination of semi-transparent objects from holographic data. *Opt. Commun.* **1,** 153–156 (1969).
8. Gabor, D. A new microscopic principle. *Nature* **161,** 777–778 (1948).
9. Popescu, G. *Quantitative Phase Imaging of Cells and Tissues* (McGraw-Hill, 2011).
10. Paganin, D. & Nugent, K. A. Noninterferometric phase imaging with partially coherent light. *Phys. Rev. Lett.* **80,** 2586–2589 (1998).
11. Marquet, P. *et al.* Digital holographic microscopy: a noninvasive contrast imaging technique allowing quantitative visualization of living cells with subwavelength axial accuracy. *Opt. Lett.* **30,** 468–470 (2005).
12. Chalut, K. J., Brown, W. J. & Wax, A. Quantitative phase microscopy with asynchronous digital holography. *Opt. Express* **15,** 3047–3052 (2007).
13. Popescu, G. *et al.* Fourier phase microscopy for investigation of biological structures and dynamics. *Opt. Lett.* **29,** 2503–2505 (2004).
14. Ikeda, T., Popescu, G., Dasari, R. R. & Feld, M. S. Hilbert phase microscopy for investigating fast dynamics in transparent systems. *Opt. Lett.* **30,** 1165–1168 (2005).
15. Popescu, G., Ikeda, T., Dasari, R. R. & Feld, M. S. Diffraction phase microscopy for quantifying cell structure and dynamics. *Opt. Lett.* **31,** 775–777 (2006).
16. Wang, Z. *et al.* Spatial light interference microscopy (SLIM). *Opt. Express* **19,** 1016–1026 (2011).
17. Rappaz, B. *et al.* Comparative study of human erythrocytes by digital holographic microscopy, confocal microscopy, and impedance volume analyzer. *Cytometry A* **73A,** 895–903 (2008).
18. Khmaladze, A., Kim, M. & Lo, C. M. Phase imaging of cells by simultaneous dual-wavelength reflection digital holography. *Opt. Express* **16,** 10900–10911 (2008).
19. Shaked, N. T., Rinehart, M. T. & Wax, A. Dual-interference-channel quantitative-phase microscopy of live cell dynamics. *Opt. Lett.* **34,** 767–769 (2009).
20. Park, Y. K. *et al.* Refractive index maps and membrane dynamics of human red blood cells parasitized by plasmodium falciparum. *Proc. Natl Acad. Sci. USA* **105,** 13730–13735 (2008).
21. Park, Y. K. *et al.* Measurement of red blood cell mechanics during morphological changes. *Proc. Natl Acad. Sci. USA* **107,** 6731–6736 (2010).
22. Mir, M. *et al.* Optical measurement of cycle-dependent cell growth. *Proc. Natl Acad. Sci. USA* **108,** 13124–13129 (2011).
23. Pavillon, N. *et al.* Early cell death detection with digital holographic microscopy. *PLoS ONE* **7,** e30912 (2012).
24. Chen, B. Q. & Stamnes, J. J. Validity of diffraction tomography based on the first Born and the first Rytov approximations. *Appl. Opt.* **37,** 2996–3006 (1998).
25. Carney, P. S., Wolf, E. & Agarwal, G. S. Diffraction tomography using power extinction measurements. *J. Opt. Soc. Am. A* **16,** 2643–2648 (1999).
26. Lauer, V. New approach to optical diffraction tomography yielding a vector equation of diffraction tomography and a novel tomographic microscope. *J. Microsc.* **205,** 165–176 (2002).
27. Charriere, F. *et al.* Living specimen tomography by digital holographic microscopy: morphometry of testate amoeba. *Opt. Express* **14,** 7005–7013 (2006).
28. Charriere, F. *et al.* Cell refractive index tomography by digital holographic microscopy. *Opt. Lett.* **31,** 178–180 (2006).
29. Choi, W. *et al.* Tomographic phase microscopy. *Nature Methods* **4,** 717–719 (2007).
30. Cotte, Y. *et al.* Marker-free phase nanoscopy. *Nature Photon.* **7,** 113–117 (2013).
31. Choi, W. S., Fang-Yen, C., Badizadegan, K., Dasari, R. R. & Feld, M. S. Extended depth of focus in tomographic phase microscopy using a propagation algorithm. *Opt. Lett.* **33,** 171–173 (2008).
32. Zhou, R., Edwards, C., Arbabi, A., Popescu, G. & Goddard, L. L. Detecting 20 nm wide defects in large area nanopatterns using optical interferometric microscopy. *Nano Lett.* **13,** 3716–3721 (2013).
33. Goodman, J. W. *Speckle Phenomena in Optics: Theory and Applications* (Roberts & Co., 2007).
34. Mir, M. *et al.* Visualizing *Escherichia coli* sub-cellular structure using sparse deconvolution spatial light interference tomography. *PLoS ONE* **7,** e39816 (2012).
35. Wang, Z. *et al.* Spatial light interference tomography (SLIT). *Opt. Express* **19,** 19907–19918 (2011).
36. Bon, P., Aknoun, S., Savatier, J., Wattellier, B. & Monneret, S. in *Three-Dimensional and Multidimensional Microscopy: Image Acquisition and Processing XX* (eds Cogswell, C. J., Brown, T. G., Conchello, J.-A. & Wilson, T.) 858–918 SPIE (2013).
37. Pawley, J. B. *Handbook of Biological Confocal Microscopy* 3rd edn (Springer, 2006).
38. Ding, H. F., Wang, Z., Nguyen, F., Boppart, S. A. & Popescu, G. Fourier transform light scattering of inhomogeneous and dynamic structures. *Phys. Rev. Lett.* **101,** 238102 (2008).
39. Chew, W. C. *Waves and Fields in Inhomogeneous Media* (IEEE Press, 1995).
40. Kim, T., Sridharan, S. & Popescu, G. in *Handbook of Coherent-Domain Optical Methods* Vol. 1 (ed. Tuchin, V. V.) Ch. 7, 259–290 (Springer, 2013).
41. Huang, D. *et al.* Optical coherence tomography. *Science* **254,** 1178–1181 (1991).
42. Ralston, T. S., Marks, D. L., Carney, P. S. & Boppart, S. A. Interferometric synthetic aperture microscopy. *Nature Phys.* **3,** 129–134 (2007).
43. Bain, B. J. *A Beginner's Guide to Blood Cells* 2nd edn (Blackwell, 2004).

44. Khairy, K., Foo, J. & Howard, J. Shapes of red blood cells: comparison of 3D confocal images with the bilayer-couple model. *Cell. Mol. Bioeng.* **1,** 173–181 (2008).
45. Babacan, S. D., Wang, Z., Do, M. & Popescu, G. Cell imaging beyond the diffraction limit using sparse deconvolution spatial light interference microscopy. *Biomed. Opt. Exp.* **2,** 1815–1827 (2011).
46. Donachie, W. D. Co-ordinate regulation of the *Escherichia coli* cell cycle or the cloud of unknowing. *Mol. Microbiol.* **40,** 779–785 (2001).
47. Raskin, D. M. & De Boer, P. A. J. Rapid pole-to-pole oscillation of a protein required for directing division to the middle of *Escherichia coli*. *Proc. Natl Acad. Sci. USA* **96,** 4971–4976 (1999).
48. Ghosh, A. S. & Young, K. D. Helical disposition of proteins and lipopolysaccharide in the outer membrane of *Escherichia coli*. *J. Bacteriol.* **187,** 1913–1922 (2005).
49. Wiener, N. Generalized harmonic analysis. *Acta Mathematica* **55,** 117–258 (1930).
50. Khintchine, A. Eine verschärfung des poincaréschen 'wiederkehrsatzes'. *Comp. Math* **1,** 177–179 (1935).

Acknowledgements
This research was supported in part by the National Science Foundation (grants CBET-1040462 MRI, CBET 08-46660 CAREER) and the Science and Technology Center for Emergent Behaviors of Integrated Cellular Systems (EBICS, CBET-0939511). The authors thank R. Bashir and K. Park for providing HT29 cells, I. Golding and M. Bednarz for providing *E. coli* cells and S. Robinson for assistance with SEM imaging of RBCs. The authors also thank J. Howard, K. Khairy and J.-J. Foo for providing confocal images of RBCs. R.Z. acknowledges support from the Beckman Foundation through a Beckman Graduate Fellowship. For more information, visit http://light.ece.illinois.edu

Author contributions
G.P., R.Z. and S.D.B. proposed the idea. G.P., R.Z., T.K. and P.S.C. developed the theoretical description of the method. T.K. and R.Z. performed three-dimensional PSF calculations. T.K. and M.M. performed quantitative phase imaging. S.D.B. and M.M. developed the sparse deconvolution method. T.K. and R.Z. performed data analysis and three-dimensional reconstruction. G.P. and L.L.G. supervised the research. All authors contributed to writing the manuscript.

Additional information
Supplementary information is available in the online version of the paper. Reprints and permissions information is available online at www.nature.com/reprints. Correspondence and requests for materials should be addressed to G.P.

Competing financial interests
G.P. has financial interest in Phi Optics, Inc., a company developing quantitative phase imaging technology for materials and life science applications, which, however, did not sponsor the research.

CORRIGENDUM

Demon-like algorithmic quantum cooling and its realization with quantum optics

Jin-Shi Xu, Man-Hong Yung, Xiao-Ye Xu, Sergio Boixo, Zheng-Wei Zhou, Chuan-Feng Li, Alán Aspuru-Guzik & Guang-Can Guo

Nature Photon. **8,** 113–118 (2014); published online 19 January 2014; corrected after print 5 February 2014

In the version of this Letter originally published online and in print, the affiliation of Sergio Boixo was incorrectly given. He is affiliated with the Department of Chemistry and Chemical Biology, Harvard University, Cambridge, Massachusetts 02138, USA. This has now been corrected in the HTML and PDF versions of this Letter.

CORRIGENDUM

Simultaneous measurement of nanoscale electric and magnetic optical fields

B. le Feber, N. Rotenberg, D. M. Beggs and L. Kuipers

Nature Photonics **8,** 43–46 (2014); published online: 15 December 2013; corrected after print: 30 January 2014

The reference section in the print version of this Letter contained the following errors:
For ref. 3, the volume number should have been 4 rather than 3.
For ref. 17, "**15,** 1289–1295" should have been "http://dx.doi.org/10.1126/science.1232009".
For ref. 30, the volume number should have been 326 rather than 23.
The online HTML and PDF versions of the Letter do not contain these errors.

nature photonics

SUPPLEMENTARY INFORMATION

DOI: 10.1038/NPHOTON.2013.350

Supplementary Information: White light diffraction tomography of unlabeled live cells

Taewoo Kim[1†], Renjie Zhou[1,2†], Mustafa Mir[1], S. Derin Babacan[3], P. Scott Carney[4], Lynford L. Goddard[2], and Gabriel Popescu[1]*

*gpopescu@illinois.edu

a. Spatial light interference microscopy (SLIM)

Spatial light interference microscopy (SLIM)[1] is a recently developed quantitative phase imaging technique, which combines Zernike's phase contrast microscopy and Gabor's holography. It is capable of measuring nanoscale structures and dynamics in live cells by generating endogenous contrast and mapping quantitative optical path-lengths at each point in the image. Figure S1a shows a schematic for the SLIM experimental setup, which is designed to be an add-on module to a commercial phase contrast microscope (Axio Observer Z1). This microscope has a motorized focus drive with a minimum step size of 10 nm and an F/0.55 motorized shutter that allows us precise z-scanning and illumination control. The back focal plane of the objective lens contains a thin metal annulus (phase ring) which provides a $\pi/2$ phase shift between the scattered and unscattered light. In SLIM, the image plane of the phase contrast microscope is first relayed and magnified through a 4*f* system (AC508-150-A1-ML 150mm doublet and AC508-200-A1-ML 200mm doublet, Thorlabs), and the back focal plane of the objective lens is imaged onto a programmable liquid crystal spatial light modulator (XY Phase Series Model P512 -635, Boulder Nonlinear Systems, Inc, USA), which is located in the Fourier plane of the second 4*f* system (AC508-300-A1-ML 300mm doublet and AC508-500-A1-ML 500mm doublet, Thorlabs). A desired ring pattern is projected onto the SLM, and is matched to the image of the ring on the SLM. In this manner the SLM is used to provide additional phase shifts of 0, $\pi/2$, π and $3\pi/2$ between the scattered and un-scattered light. These four phase shifted interferograms are recorded at the image plane (at the focus of the second Fourier lens) using a CCD detector (AxioCam MRm, Zeiss). The SLM, CCD, and microscope are synchronized through a custom LabVIEW program. In SLIM we acquire 8 fps, which translates to 2 quantitative phase images (QPI) per second. This acquisition rate is limited by the frame rate of the CCD and the refresh rate of SLM. Therefore, for example, a z-stack of 100 slices can be obtained in 50 seconds. By using these four interferograms, the actual phase shift caused by the sample can be uniquely determined within a range of 2π. Any 2π ambiguities are corrected by Goldstein's unwrapping algorithm.

The broadband source (12V, 100W Hal, square filament, Zeiss) with a temporal coherence length of 1.2μm takes a significant role in increasing resolution since it does not suffer from speckle, and thus, improves the sensitivity (0.029nm temporal and 0.28nm spatial sensitivities). Also, since SLIM is built as an add-on module to a commercial microscope, it is possible to overlay SLIM with other microscopy modalities (e.g. epi-fluorescence, DIC). With these features, SLIM is capable of performing multimodal and functional studies[2-9]. Furthermore, with the short coherence length and a high numerical aperture objective, SLIM provides excellent depth

DOI: 10.1038/NPHOTON.2013.350

sectioning (1.2 μm depth sectioning for a 63x/1.4NA objective), which plays a large role in our reconstruction method.

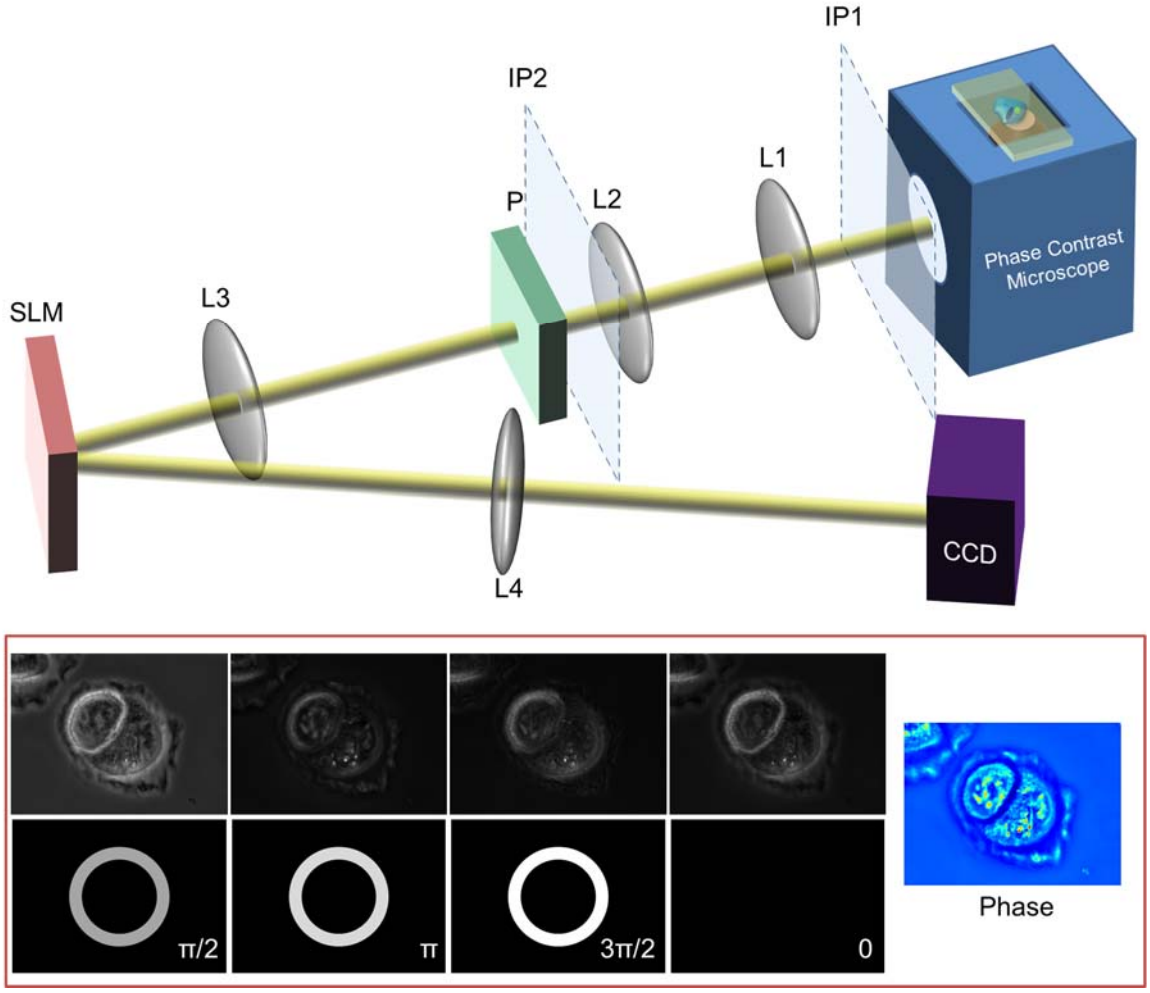

Figure S1. Illustration the SLIM module and the phase image measurement. (top) A schematic of SLIM setup built as an add-on module to a commercial phase contrast microscope. L1 (f = 150mm) and L2 (f = 200mm) forms a 4f system, which relays the image plane of the microscope (IP1) to a new image plane (IP2) so that the modulation at the spatial light modulator (SLM) can be optimized. The polarizer (P) aligns the polarization of the field with the slow axis of the SLM. L3 (f = 300mm) and L4 (f = 500mm) forms another 4f system, where the SLM is at the Fourier plane and the CCD is at the relayed image plane. (bottom) 4 different phase shifted images shown with the illustrations of corresponding phase pattern on the SLM. SLIM measures the phase of the object by combining these four frames.

Here we provide additional explanation of SLIM's imaging principle. We first define the temporal cross-correlation function, $\Gamma_{12}(\mathbf{r},\tau)$, as[9, 10]

$$\Gamma_{12}(\mathbf{r},\tau) = \left\langle U_s(\mathbf{r},t)U_r^*(\mathbf{r},t+\tau)\right\rangle, \qquad \text{(a1)}$$

where U_s and U_r are the scattered and the reference (unscattered) field, respectively. $\Gamma_{12}(\mathbf{r},\tau)$ is a complex function that can be written as

$$\Gamma_{12}(\mathbf{r},\tau)=\left|\Gamma_{12}(\mathbf{r},\tau)\right|e^{i\phi(\mathbf{r},\tau)}, \tag{a2}$$

where $\phi(\mathbf{r},\tau)$ is the phase associated with the image field, which we measure in SLIM using the four phase shifted interferograms. The generalized Wiener-Khintchine theorem[10, 11] allows us to relate $\Gamma_{12}(\mathbf{r},\tau)$ to the cross-spectral density through Fourier transform of

$$\Gamma_{12}(\mathbf{r},\tau)=\int_0^\infty W_{12}(\mathbf{r},\omega)e^{i\omega\tau}d\omega, \tag{a3}$$

where

$$W_{12}(\mathbf{r},\omega)=\left\langle U_s(\mathbf{r},\omega)U_r^*(\mathbf{r},\omega)\right\rangle. \tag{a4}$$

During the phase shifting measurement, $\Gamma_{12}(\mathbf{r},\tau)$ is evaluated at $\tau=0$, which allows us to write

$$\Gamma_{12}(\mathbf{r},\tau=0)=\int_0^\infty \left\langle U_s(\mathbf{r},\omega)U_r^*(\mathbf{r},\omega)\right\rangle d\omega. \tag{a5}$$

We see from Eq. (a5) that the unknown quantity is the scattered field, U_s. In the next section, we first derive an analytical solution for U_s and then establish the relationship between the measurable quantity, Γ_{12}, and the 3D object structure of interest.

b. White light diffraction tomography (WDT)

The inhomogeneous Helmholtz equation, which describes the field U in a medium with index distribution of $n(\mathbf{r})$ is

$$\nabla^2U(\mathbf{r},\omega)+n^2(\mathbf{r},\omega)\beta_0^2(\omega)U(\mathbf{r},\omega)=0, \tag{b1}$$

where $\beta_0(\omega)=\omega/c$ is the wavenumber in vacuum. We re-arrange Eq. (b1) as

$$\nabla^2U(\mathbf{r},\omega)+\beta^2(\omega)U(\mathbf{r},\omega)=-\chi(\mathbf{r},\omega)\beta_o^2(\omega)U(\mathbf{r},\omega), \tag{b2}$$

where $\beta(\omega)=\bar{n}\beta_0(\omega)$ (we assume non-dispersive objects), $\bar{n}=\left\langle n(\mathbf{r})\right\rangle_r$ is the spatially averaged refractive index, and $\chi(\mathbf{r},\omega)=n^2(\mathbf{r},\omega)-\bar{n}^2(\omega)$ is the scattering potential. The total field $U(\mathbf{r},\omega)$ can be written as $U(\mathbf{r},\omega)=U_i(\mathbf{r},\omega)+U_s(\mathbf{r},\omega)$, where $U_i(\mathbf{r},\omega)$ is the incident wave. U_i satisfies the homogeneous wave equation,

$$\nabla^2U_i(\mathbf{r},\omega)+\beta^2(\omega)U_i(\mathbf{r},\omega)=0. \tag{b3}$$

Equation (b3) has a plane-wave solution $U_i(\mathbf{r},\omega)=A(\omega)e^{i\beta(\omega)z}$ where $A(\omega)$ is the spectral amplitude of the incident field. Subtracting Eq. (b2) from Eq. (b3) gives

$$\nabla^2U_s(\mathbf{r},\omega)+\beta^2(\omega)U_s(\mathbf{r},\omega)=-\chi(\mathbf{r})\beta_o^2(\omega)U(\mathbf{r},\omega). \tag{b4}$$

DOI: 10.1038/NPHOTON.2013.350

From Eq. (b4) we can clearly see that the driving term of the right hand side represents the interaction of the object scattering potential χ with the total field U. Under the first Born approximation, i.e., $\left|U_s(\mathbf{r},\omega)\right| << \left|U_i(\mathbf{r},\omega)\right|$, we can approximate $U(\mathbf{r},\omega)$ on the right hand side as $U_i(\mathbf{r},\omega)$, allowing Eq. (b4) to be re-written as,

$$\nabla^2 U_s(\mathbf{r},\omega) + \beta^2(\omega) U_s(\mathbf{r},\omega) = -\chi(\mathbf{r},\omega)\beta_o^2(\omega) A(\omega) e^{i\beta(\omega)z}. \qquad \text{(b5)}$$

Instead of employing the traditional Green's function approach and the angular spectrum representation (Weyl's formula), we solve for the scattered field directly in the wavevector space, using the 3D Fourier transformation. We first perform a 3D Fourier transform of Eq. (b5), which yields

$$\left[\beta^2(\omega) - k^2\right] U_s(\mathbf{k},\omega) = -\beta_0^2(\omega) A(\omega) \chi\left[\mathbf{k}_\perp, k_z - \beta(\omega)\right]. \qquad \text{(b6)}$$

In Eq. (b6), we used the *shift theorem* of Fourier transforms, namely, $\chi(\mathbf{r},\omega)e^{i\beta(\omega)z} \rightarrow \chi\left[\mathbf{k}_\perp, k_z - \beta(\omega)\right]$, where the arrow indicates Fourier transformation. Note that, throughout the manuscript, we use the same symbol for a function and its Fourier transform but carry all the arguments explicitly, which clearly identifies the domain in which the function operates. For example, $\chi(\mathbf{k})$ is the Fourier transform of $\chi(\mathbf{r})$.

From Eq. (b6), the scattered field U_s is obtained immediately,

$$U_s(\mathbf{k},\omega) = -\beta_0^2(\omega) A(\omega) \frac{\chi\left[\mathbf{k}_\perp, k_z - \beta(\omega)\right]}{\beta^2(\omega) - k_\perp^2 - k_z^2}. \qquad \text{(b7)}$$

Next, we derive an expression for the field as a function of axial distance z, i.e., we arrange the terms such that a 1D inverse Fourier transform with respect to k_z can be easily performed. Toward this end, we define a $k_\perp$-dependent propagation constant, $q = \sqrt{\beta^2(\omega) - k_\perp^2}$, and re-write Eq. (b7) as

$$U_s(\mathbf{k},\omega) = -\beta_0^2(\omega) A(\omega) \chi\left[\mathbf{k}_\perp, k_z - \beta(\omega)\right] \frac{1}{2q}\left(\frac{1}{k_z - q} - \frac{1}{k_z + q}\right). \qquad \text{(b8)}$$

Since our imaging experiment only measures the transmitted field or the forward scattered field, we ignore the backscattered field, $\frac{1}{k_z + q}$. We perform an inverse Fourier transform on Eq. (b8) with respect to k_z in order to obtain the forward scattered field as a function of transverse wavevector, $\mathbf{k}_\perp$, axial distance, z, and angular frequency, ω

$$U_s(\mathbf{k}_\perp, z; \omega) = -\frac{\beta_0^2(\omega) A(\omega)}{2q}\left[\chi(\mathbf{k}_\perp, z) e^{i\beta(\omega)z}\right] \circledv_z e^{iqz}. \qquad \text{(b9)}$$

In Eq. (b9), $\circledv_z$ indicates convolution along the z-dimension, $f(z)\circledv_z e^{iqz} = \int_{-\infty}^{\infty} f(z')e^{iq(z-z')}dz'$. It can be easily seen that the convolution of a function with a complex exponential yields the Fourier transform of that function multiplied the complex exponential, which yields the simple result $\left[\chi\left(\mathbf{k}_\perp, z;\omega\right)e^{i\beta(\omega)z}\right]\circledv_z e^{iqz} = e^{iqz}\chi\left[\mathbf{k}_\perp, q-\beta\left(\omega\right)\right]$.

In order to insert the result of Eq. (b9) into Eq. (a5), we need to Fourier transform $\Gamma_{12}\left(\mathbf{r},\tau\right)$ with respect to the transverse position vector, $\mathbf{r}_\perp = (x,y)$. Since $U_r\left(\mathbf{r},\omega\right)$ is a plane wave propagating in z-direction, Eq. (a4) in $\mathbf{k}_\perp$-space is

$$W_{12}\left(\mathbf{k}_\perp, z, \omega\right) = \left\langle U_s\left(\mathbf{k}_\perp, z, \omega\right)U_r^*\left(z,\omega\right)\right\rangle. \tag{b10}$$

Using the solution of U_s from Eq. (b9) and $U_r\left(z,\omega\right) = A\left(\omega\right)e^{i\beta(\omega)z}$, we have

$$W_{12}\left(\mathbf{k}_\perp, z, \omega\right) = \frac{-\beta_o^2\left(\omega\right)S\left(\omega\right)e^{iz\left[q-\beta(\omega)\right]}}{2q}\chi\left[\mathbf{k}_\perp, q-\beta\left(\omega\right)\right], \tag{b11}$$

where $S\left(\omega\right) = \left|A\left(\omega\right)\right|^2$ is the power spectrum of the illumination field. Using Eq. (a5) we obtain the temporal cross correlation at zero-delay as a function of the frequency integral

$$\Gamma_{12}\left(\mathbf{k}_\perp, z, 0\right) = -\int_0^\infty \frac{\beta_o^2\left(\omega\right)S\left(\omega\right)e^{iz\left[q-\beta(\omega)\right]}}{2q}\chi\left[\mathbf{k}_\perp, q-\beta\left(\omega\right)\right]d\omega. \tag{b12}$$

With the relation $\beta(\omega) = \bar{n}\beta_0 = \bar{n}\omega/c$, we can change the integral from $d\omega$ to $d\beta$, $S\left(\omega\right)$ to $S\left(\beta c/\bar{n}\right)$, such that Eq. (b12) becomes

$$\Gamma_{12}\left(\mathbf{k}_\perp, z, 0\right) = -\frac{c}{2\bar{n}^3}\int_0^\infty \frac{\beta^2 S\left(\beta c/\bar{n}\right)e^{iz(q-\beta)}}{q}\chi\left(\mathbf{k}_\perp, q-\beta\right)d\beta. \tag{b13}$$

Experimentally, we measure $S\left(\lambda\right)$. So to obtain the spectrum distribution for $S\left(\beta c/\bar{n}\right)$ from $S\left(\lambda\right)$, we need to consider the Jacobian transformations, $S\left(\beta c/\bar{n}\right) \leftrightarrow \bar{n}S\left(\beta\right)/c$ and $S\left(\beta\right) \leftrightarrow \lambda^2 S\left(\lambda\right)/2\pi$. In order to evaluate the integral in Eq. (b13), we define a new variable $Q = q-\beta = \sqrt{\beta^2 - k_\perp^2} - \beta$, from which we have $\beta = -\frac{Q^2+k_\perp^2}{2Q}$ and $q = \left(-\frac{Q}{2} + \frac{k_\perp^2}{2Q}\right)$. Substituting $d\beta$ for dQ, we need to consider the Jacobian $\frac{d\beta}{dQ} = \left(-\frac{1}{2} + \frac{k_\perp^2}{2Q^2}\right)$, then Eq. (b13) becomes

DOI: 10.1038/NPHOTON.2013.350

$$\Gamma_{12}(\mathbf{k}_\perp, z; 0) = \frac{1}{8\bar{n}^2}\int_0^\infty \frac{\left(Q^2 + k_\perp^2\right)^2}{Q^3} S\left(-\frac{Q^2 + k_\perp^2}{2Q}\right)\chi(\mathbf{k}_\perp, Q)e^{izQ}dQ$$
$$= \frac{1}{8\bar{n}^2} FT_Q^{-1}\left[\frac{\left(Q^2 + k_\perp^2\right)^2}{Q^3} S\left(-\frac{Q^2 + k_\perp^2}{2Q}\right)\right] \circledv_z \chi(\mathbf{k}_\perp, -z). \qquad \text{(b14)}$$
$$= \Sigma(\mathbf{k}_\perp, -z) \circledv_z \chi(\mathbf{k}_\perp, -z)$$

In Eq. (b14), Σ is the function that incorporates all the details of the instrument response. Note that the $\mathbf{k}_\perp$ coverage of Σ is limited to a maximum value $\mathbf{k}_\perp^{\max} = \beta_0 NA$, where NA is the numerical aperture of the objective. By measuring z-stacks in SLIM, we can reconstruct the object's 3D distribution through deconvolution of Eq. (b14). Alternatively, we can write Eq. (b14) in the spatial frequency domain as a product, namely,

$$\Gamma_{12}(\mathbf{k}_\perp, Q; 0) = \Sigma(\mathbf{k}_\perp, Q)\chi(\mathbf{k}_\perp, Q), \qquad \text{(b15)}$$

where,

$$\Sigma(\mathbf{k}_\perp, Q) = \frac{1}{8\bar{n}^2}\frac{\left(Q^2 + k_\perp^2\right)^2}{Q^3} S\left(-\frac{Q^2 + k_\perp^2}{2Q}\right). \qquad \text{(b16)}$$

c. Point spread function calculation

Notice that Eq. (b16) gives the *coherent transfer function* or the Fourier transform of the point spread function (PSF) of the imaging system. Therefore, by measuring the source spectrum and filtering according to the NA of the objective, the coherent transfer function of the system can be calculated directly.

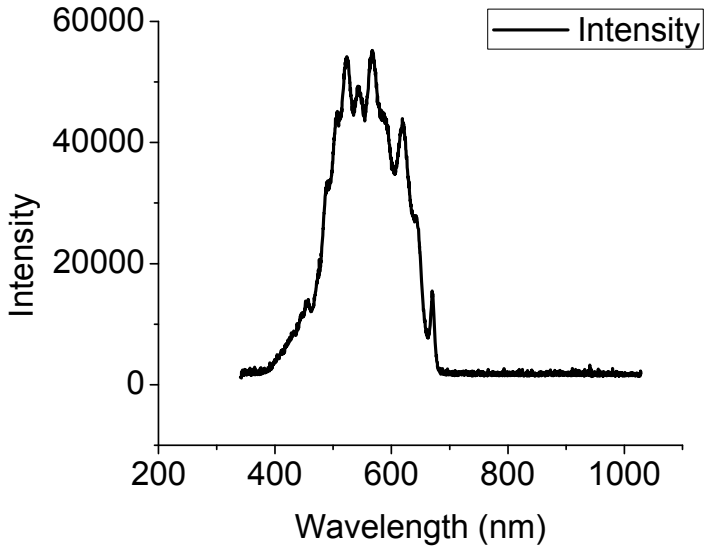

Figure S2. Spectrum of the white light source for SLIM, measured over the range of 340nm to 1028nm. The y-axis is in arbitrary units.

First, the optical spectrum (Fig. S2) of the lamp (12V, 100W Hal, square filament, Zeiss) is measured at 3200K using a fiber optic spectrometer (Ocean Optics USB2000+ Fiber Optic Spectrometer). Since the spectrum is measured as $S(\lambda)$ in air, we perform the Jacobian transformation introduced in the previous section to obtain the spectrum in terms of variable $\beta = -\left(Q^2 + k_\perp^2\right)/2Q$. Next through numerical calculations, this spectrum is resampled onto a 3D grid in spatial-frequency space (k_x, k_y, Q). For a 63x/1.4NA objective, each pixel in space corresponds to 45 nm and each z-slice is separated by 200 nm. Because of the quadratic relationship between Q and β, the resampling yields two duplicates of the spectrum. Therefore, the second of the two duplicates which appears at high Q is removed by applying a spatial low-pass filter with cutoff $Q = k_\perp$. Further filtering in Q is performed to incorporate the physical minimum and maximum value of Q and the maximum $k_\perp$ value, which is determined by the NA of the objective, $k_\perp^{\max} = \beta_0 NA$. In order to avoid well known numerical artifacts due to sharp cutoffs in the frequency domain, we used a simple apodization procedure to smooth the edges of the filter function. Thus, we convolved the filter function with a narrow Gaussian function, of a width that is 5% of the system's maximum transverse frequency, $k_\perp^{\max}$. Finally, the coherent transfer function (shown in Figs. 2b-c), is Fourier transformed to obtain the PSF. Figures S3a-b show the phase of the complex PSF (top row from WDT, middle row from measurement, and bottom row from deconvolving the measurement with the PSF from WDT), which was normalized and thresholded to suppress side lobes. This complex PSF was used for the 3D reconstruction, as detailed below.

d. Deconvolution algorithm

SLIM measures the 3D complex field distribution, i.e. phase and amplitude, which can be expressed as a convolution between the point spread function (PSF) of the imaging system, $\Sigma(\mathbf{r})$, and the structure of the object, $\chi(\mathbf{r}) = n^2(\mathbf{r}) - \bar{n}^2$. We represent the real field as a complex analytic signal, $\bar{U}(\mathbf{r}) = \chi(\mathbf{r}) \textcircled{v} \Sigma(\mathbf{r}) + \zeta(\mathbf{r})$, which also contains a signal independent noise term, $\zeta(\mathbf{r})$. Considering a weakly scattering phase object with very small absorption, where most of the useful information is contained in the phase image, it is reasonable to assume that the amplitude of the field is constant over the entire space. Therefore, the deconvolution can be performed on the phase term only, $\exp\left[i\Phi(\mathbf{r})\right]$. The function that our algorithm minimizes is

$$\hat{\Phi}(\mathbf{r}) = \arg\min_{\Phi(\mathbf{r})} \frac{1}{2\sigma^2} \left\| \exp\left[i\bar{\Phi}(\mathbf{r})\right] - \Sigma(\mathbf{r}) \textcircled{v} \exp\left[i\Phi(\mathbf{r})\right] \right\|^2 + \rho R\left[\Phi(\mathbf{r})\right] \qquad \text{(d1)}$$

where σ^2 is the noise variance, ρ is the regularization parameter, and R is the regularization functional. For simplification, these purely phase-dependent fields can be expressed in vector forms.

DOI: 10.1038/NPHOTON.2013.350

$$\hat{\mathbf{f}} = \arg\min_{\mathbf{f}} \frac{1}{2\sigma^2}\left\|\mathbf{g}-\boldsymbol{\Sigma}\mathbf{f}\right\|^2 + \rho R(\mathbf{f}) \tag{d2}$$

where $\mathbf{g}$ represents the measured field, $\exp\left[i\bar{\Phi}(\mathbf{r})\right]$, $\mathbf{f}$ represents the unknown field from the structure, $\exp\left[i\Phi(\mathbf{r})\right]$, and $\boldsymbol{\Sigma}$ represents the convolution matrix corresponding to the PSF.

Phase contrast (PC) images are highly sensitive to the sharp object boundaries, but not to slow variations in the background region. For small scale objects, such as a biological cell, these characteristics of PC allows us to use the sparse representation[12], which has been used to solve a number of imaging problems[3, 13, 14], and also has been shown to generally have superior performance to classical deconvolution methods[13, 15]. When an appropriate transform is applied to a phase image, only a few of the transform coefficients contain most of the signal energy while all the other coefficients become very small. This situation is known as *transform sparsity*. In our work, the first- and second-order directional difference operators, $\begin{bmatrix}-1 & 1\end{bmatrix}$ and $\begin{bmatrix}-1 & 2 & -1\end{bmatrix}$, along with 45° and -45° first-order derivative filters, $\begin{bmatrix}-1 & 0\\ 0 & 1\end{bmatrix}$ and $\begin{bmatrix}0 & -1\\ 1 & 0\end{bmatrix}$, are used as transforms. For each plane in the image, *x*-*y*, *y*-*z* and *z*-*x*, these 2D transforms are applied and total of 12 transforms are generated to hold the spatial variations. Therefore, by applying the sparse deconvolution principle with these filters, the problem in Eq. (d2) can be expressed as

$$\hat{\mathbf{f}}, \hat{\alpha}_{ki} = \arg\min_{\mathbf{f},\alpha_{ki}} \frac{1}{\sigma^2}\left\|\mathbf{g}-\boldsymbol{\Sigma}\mathbf{f}\right\|^2 + \sum_k \left(\mathbf{D}_k\mathbf{f}\right)^T \mathbf{A}_k \left(\mathbf{D}_k\mathbf{f}\right) \tag{d3}$$

where α_{ki} are the weighting coefficients for each plane, i, $\mathbf{D}_k$ are the transform matrices, and $\mathbf{A}_k$ are diagonal matrices with α_{ki} in the diagonal. This problem is solved by an alternating iterative minimization scheme where only one unknown is estimated at a time while others are fixed. As a result, the complex image $\mathbf{f}$ is estimated by taking derivative of Eq. (d3) and setting it to zero. Therefore, the solution is of the structure is,

$$\hat{\mathbf{f}} = \left(\boldsymbol{\Sigma}^T\boldsymbol{\Sigma} + \sigma^2\sum_k \mathbf{D}_k^T\mathbf{A}_k\mathbf{D}_k\right)^{-1}\boldsymbol{\Sigma}^T\mathbf{g} \tag{d4}$$

and the weighting coefficients are estimated to be,

$$\hat{\alpha}_{ki} = \frac{1}{\left|(\mathbf{D}_k\hat{\mathbf{f}})\right|_i^2 + \varepsilon} \tag{d5}$$

where ε is a small number (10^{-9} in our case) used to avoid the trivial solution.

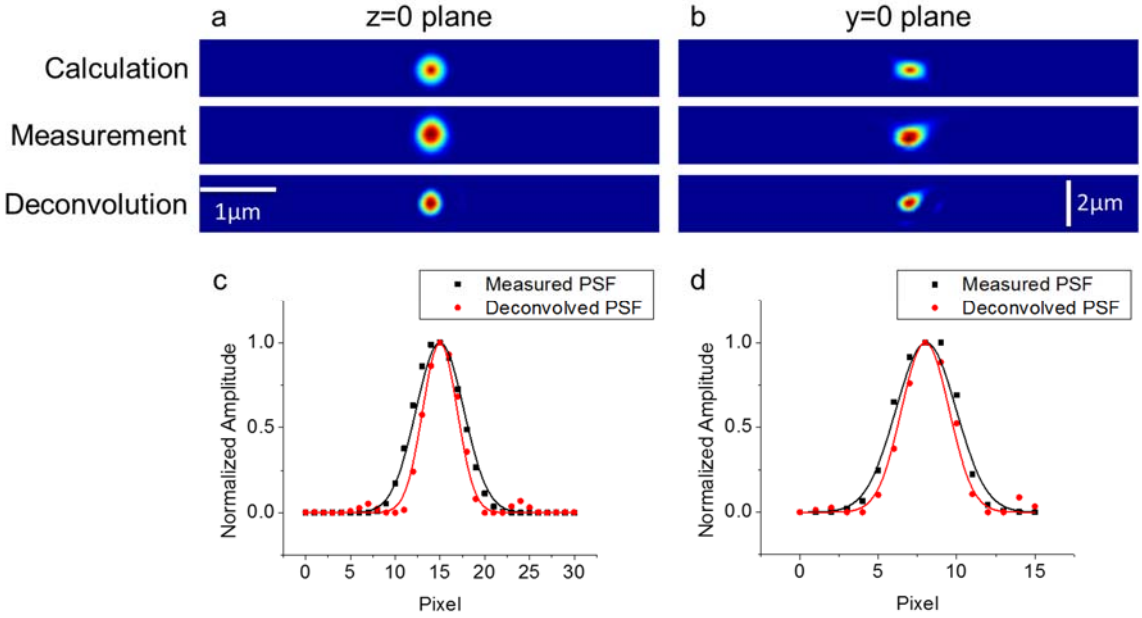

Figure S3. Point spread function profiles and resolution improvement. (a) Point spread function in the z=0 plane, showing the calculated result, measurement, and the deconvolved measured PSF using the calculated PSF. (b) Point spread function in the y=0 plane, showing the calculated result, measurement, and the deconvolved measured PSF using the calculated PSF. (c) Profile of the measured PSF and the deconvolved PSF in x-direction, which shows FWHM decrease from 398nm to 285nm. (d) Profile of the measured PSF and the deconvolved PSF in z-direction, which shows FWHM decrease from 1218nm to 967nm.

Using this approach, first a deconvolution of the measured point spread function is performed using the theoretical PSF corresponding to the 63x/1.4NA Oil Ph3 M27 objective. In the ideal case, the resolution gain should be very high so that the deconvolved PSF essentially reaches a spatial delta function. However, because of the differences between the measured PSF and theoretical PSF which comes from the lack of incorporation of errors and aberrations, the resolution gain is 1.39x in the transverse dimension (FWHM decreases from 398nm to 285nm) and 1.26x in the vertical dimension (FWHM decreases from 1218nm to 967nm). Figure S3 illustrates this increase in resolution.

For the red blood cell in Fig. 3, which is measured with a 40x/0.75NA phase contrast objective, a new PSF is calculated for deconvolution and the deconvolution is performed on a z-stack image of 128x128x100 pixels. The deconvolution process took approximately 5 minutes. The E. Coli cell reconstruction in Fig. 4 was obtained using the PSF for the 63x/1.4NA objective and a z-stack image of 128x128x17pixels, which took approximately 3 minutes for deconvolution. Due to the large size of the z-stack 640x640x140 for the HT29 cell in Fig. 5, we first split the original z-stack into 5x5 smaller z-stacks (192x192x140), each padded with 32 zero-valued pixels on each side to increase spatial sampling. For each smaller z-stack, the sparse deconvolution is applied using the 63x/1.4NA PSF. Overall, the deconvolution process for all 25 stacks took approximately one hour. Then the center region (128x128x140) of each z-stack is obtained, renormalized, and stitched together to obtain the full deconvolved image.

DOI: 10.1038/NPHOTON.2013.350

e. 3D rendering

For Figs. 2b, 3b and 4c, specific color schemes are used so that the background of the image where the value of 0 corresponds to black. Then the 3D rendering is done in ImageJ with ImageJ 3D viewer plug-in using a sampling rate of 1. For Fig. 5c, each slice in the z-stack is false-colored depending on the spatial separation and the gray value of each structure and then merged back together to one z-stack. Again, 3D rendering is done in ImageJ with the ImageJ 3D viewer plug-in using a sampling rate of 1.

f. Cell preparation and imaging

E. coli MG1655 cells are cultured in Luria Broth and then sub-cultured by 100x dilution into commercial M9CA media with Thiamine (Teknova M8010) until they reach an optical density of ~0.2. The cells are then concentrated to an optical density of ~0.4 and 2 μL of the culture is pipetted onto a glass bottom dish (In Vitro Scientific D29-21-1-N) and covered by a 1mm thick agar slab (1.5% Agarose, M9CA media). In order to mitigate drying of the agar, 70 μL of H_2O is carefully pipetted onto the edge of the dish, ensuring that it never makes contact with the sample. The dish is then covered with a circular coverslip to reduce the effects of evaporation.

Human colon adenocarcinoma (HT29) cells were cultured in DMEM (Sigma Aldrich) with 10% fetal bovine serum at 37°C with 5% CO_2. A glass bottom dish was functionalized with collagen type I solution (100μg/mL) for 30 minutes at 37°C. The cells were plated on a glass bottom dish and fixed with 4% paraformaldehyde in PBS for 30 minutes prior to the imaging, which is performed in L-15 (Sigma Aldrich) with 30% fetal bovine serum to ensure the same optical properties of the media.

In order to control the environment while imaging live cells, an incubator (XL S1 W/CO2 kit, Zeiss) and a heating insert (P S1/Scan stage, Zeiss) were used.

g. WDT imaging for an extended time period

In order to show the capability of long-period measurement of WDT, here we show the result from imaging a HeLa cell using WDT. HeLa cells are prepared in a 35mm glass bottom dish (MatTek, P35G-1.0-14-C, uncoated) with Eagle's minimum essential medium (EMEM, ATCC, 30-2003) mixed with 10% fetal bovine serum (FBS, ATCC, 30-2020). This dish is then kept in the incubator (37°C, 5% CO_2) in order for the cells to adhere to the dish and settle. Throughout imaging, the same environment is provided to the sample using the incubator (XL S1 W/CO2 kit, Zeiss) and a heating insert (P S1/Scan stage, Zeiss).

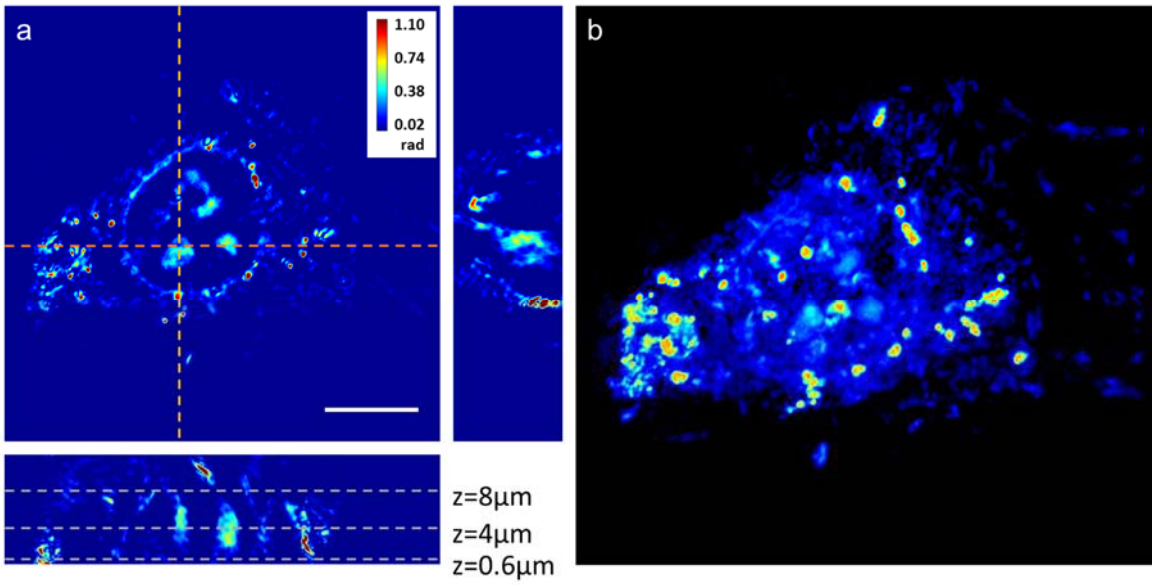

Figure S4. WDT reconstruction of a HeLa cell measured at 2 hours into the measurement over extended period of time. (a) z-stack after the reconstruction represented by its sections: (center) *x*-*y* plane taken at $z = 4$ µm from the bottom of the cell, (right) *y*-*z* section taken at the orange dashed line indicated on the center figure, (bottom) *x*-*z* section taken at the red dashed line indicated on the center figure. (b) 3D rendering of the same z-stack (Media S1). The scale bar in indicates 10 µm in sample plane.

SLIM measurement was performed every hour, taking a z-stack of 100 quantitative images each separated by 0.2 µm in depth. Figure S4a shows a z-stack taken at 2 hours into the measurement, represented by its sections through *x*, *y*, and *z*. This z-stack is then rendered using ImageJ 3D project module to record a 360° rotation of the cell in 3D (Fig. S4b). The same measurement process was taken place every hour, capturing the cell over time for 24 hours. Importantly, the HeLa culture was kept on the stage of the microscope during this 24 hour period without being disturbed or dying because of the well-controlled environment. Figures S5, S6 and S7 show the images over time, taken at certain z-positions (indicated in the bottom figure of Fig. S4a) from 25 separate z-stacks. Notice that for each of these images, we can observe active movements of the cell, and even the increase in the number of nucleoli, which indicates the viability of the cell under this environment, therefore the capacity of WDT imaging over an extended period of time.

DOI: 10.1038/NPHOTON.2013.350

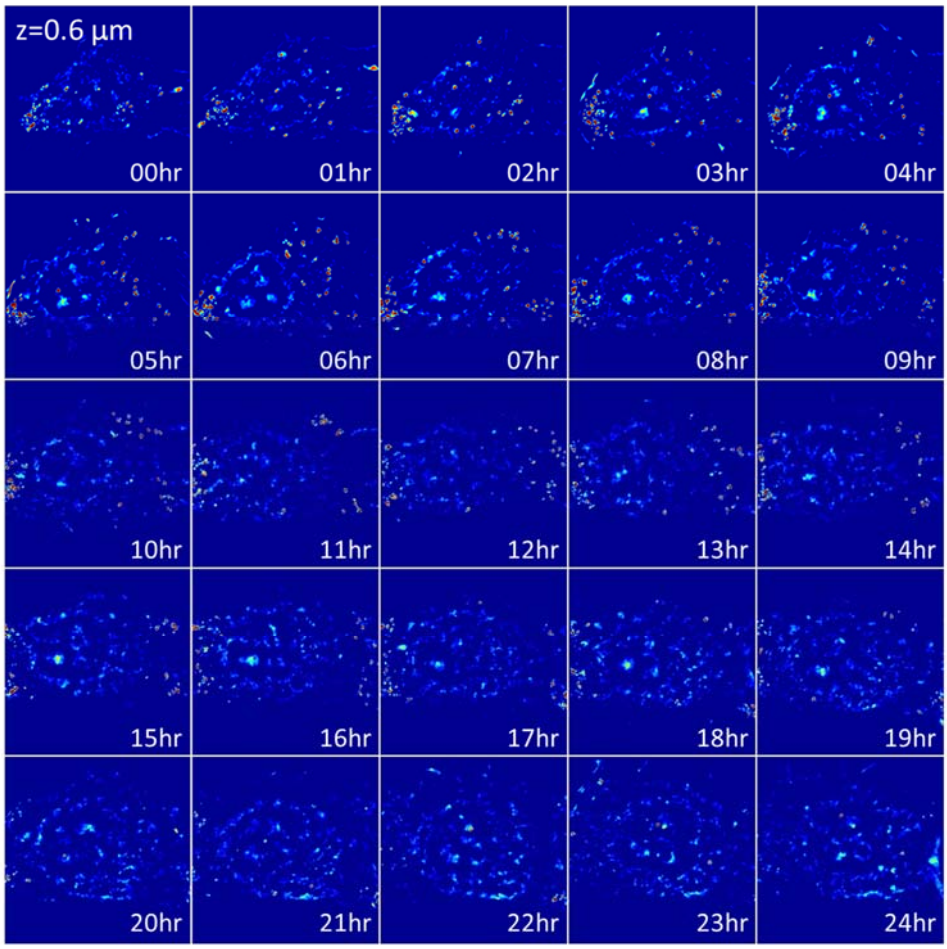

Figure S5. WDT image of HeLa cell shown by its *x*-*y* section taken at z = 0.6 µm from the bottom of the cell, where the bottom of the cell membrane and spiculate structure around it is shown. Each of the 25 images shares the same field of view as Fig. S4a and also the color bar.

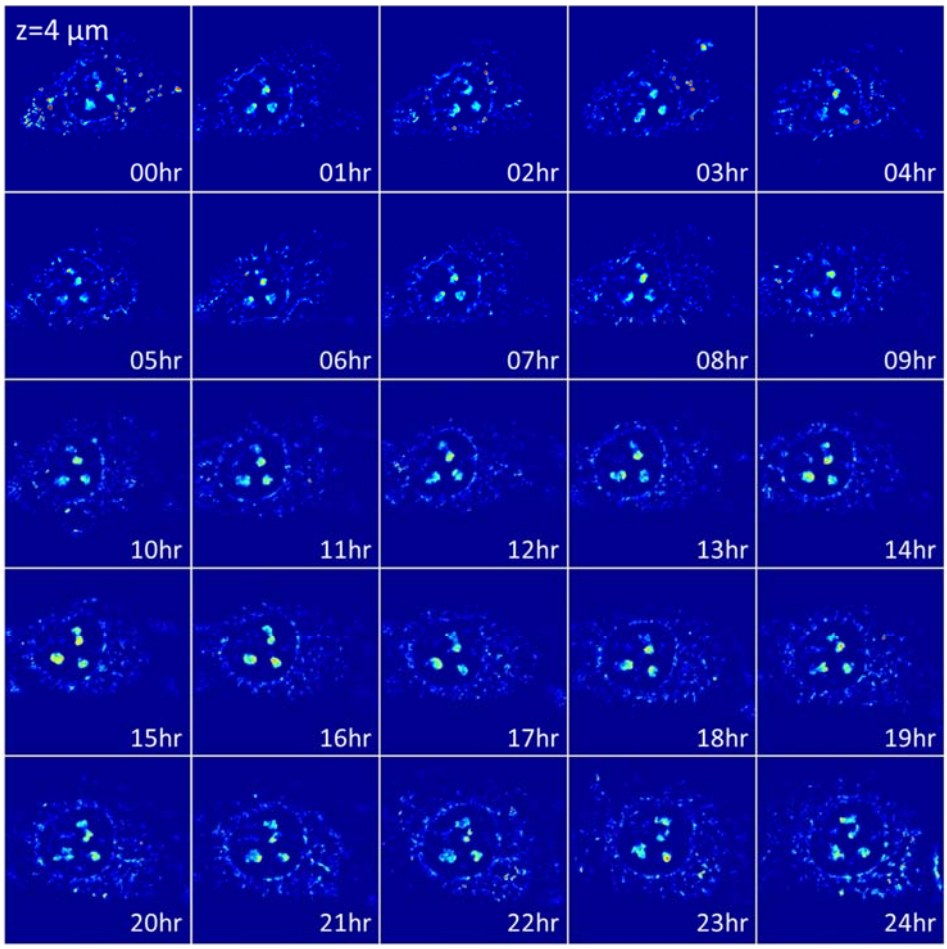

Figure S6. WDT image of HeLa cell shown by its *x*-*y* section taken at z = 4 µm from the bottom of the cell, where the nucleoli is clearly shown. Increase in the number of nucleoli shows that the cell is in a proper environment to grow and is in the process of division. Each of the 25 images shares the same field of view as Fig. S4a and also the color bar.

DOI: 10.1038/NPHOTON.2013.350

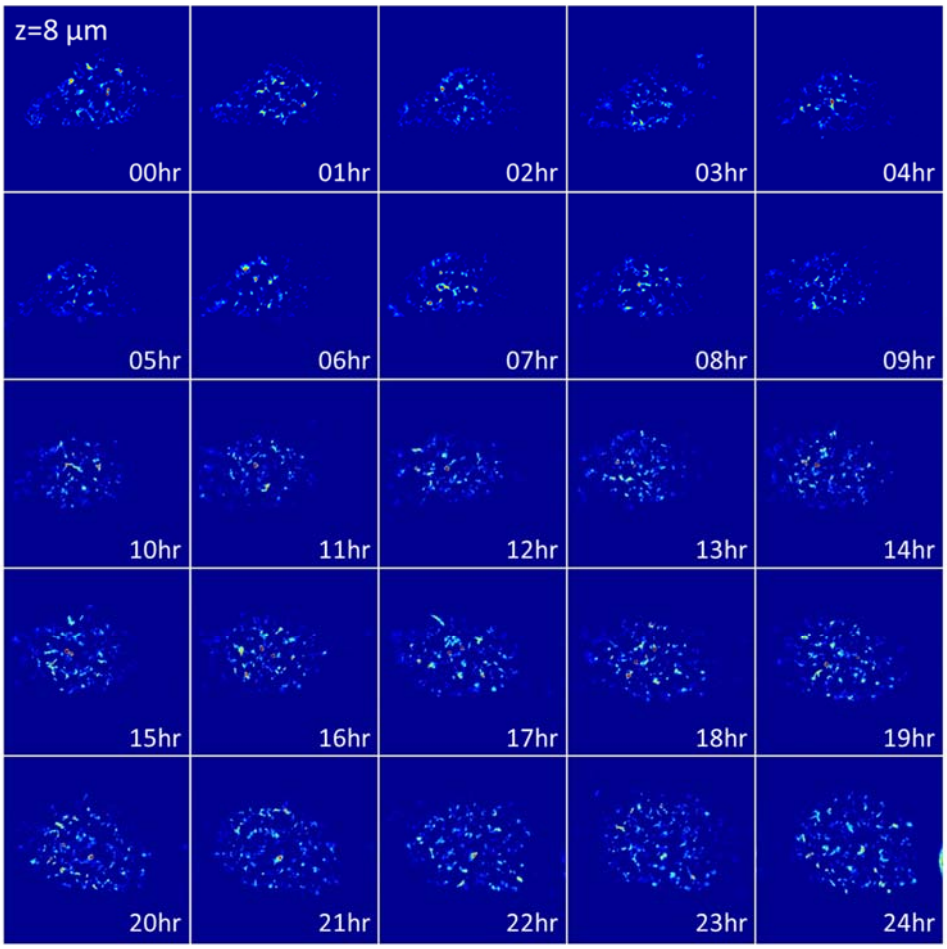

Figure S7. WDT image of HeLa cell shown by its *x*-*y* section taken at z = 8 µm from the bottom of the cell, where the top of the cell membrane is shown. Each of the 25 images shares the same field of view as Fig. S4a and also the color bar.

h. WDT imaging of 1 µm polystyrene microbeads

1 µm polystyrene beads (Thermo Scientific™ 5000 Series Polymer Particle Suspensions, 5100A. n_b = 1.59) immersed in microscope objective immersion oil (n_o = 1.516) is imaged using WDT. The sample is prepared by drying the aqueous suspension of 1µm polystyrene beads to evaporate the water on a glass cover slip, and then re-suspending the dry beads by applying the immersion oil on top of the dry beads, which is then covered by another cover slip. WDT imaging is done with 60 ms exposure time and 200 nm step size between each slice for 128 slices. The images are then reconstructed into quantitative phase images, and deconvolved using the PSF calculated using the WDT theory in order to obtain a quantitative phase tomogram. The phase tomogram is then converted to show the height, h, of the sample using the equation, $h = \lambda\Delta\phi/2\pi(n_b - n_o)$, where λ is the mean illumination wavelength and $\Delta\phi$ is the measured quantitative phase shift. Figure S8 shows the reconstructed tomogram of the bead sample, where we can clearly see two beads in a different z-plane. Figures S8a and S8b show two different focal positions that are 1.6 µm (8 slices) away from each other, where each of the two beads is in focus. Figures S8c is the resliced view of

the bead on the top left of Fig. S8a, and Fig. S8d is the resliced view of the bead on the bottom right of Fig. S8b. After the deconvolution, the longitudinal FWHM of the bead in Fig. S8d is 1.27 μm, which is much less than the sum of the size of the bead (1 μm) and the width of the PSF of the system (0.89 μm). The elongation is expected since the axial resolution is 2.6X worse compared with the transverse resolution (350 nm in transverse vs. 890 nm in axial for WDT system).

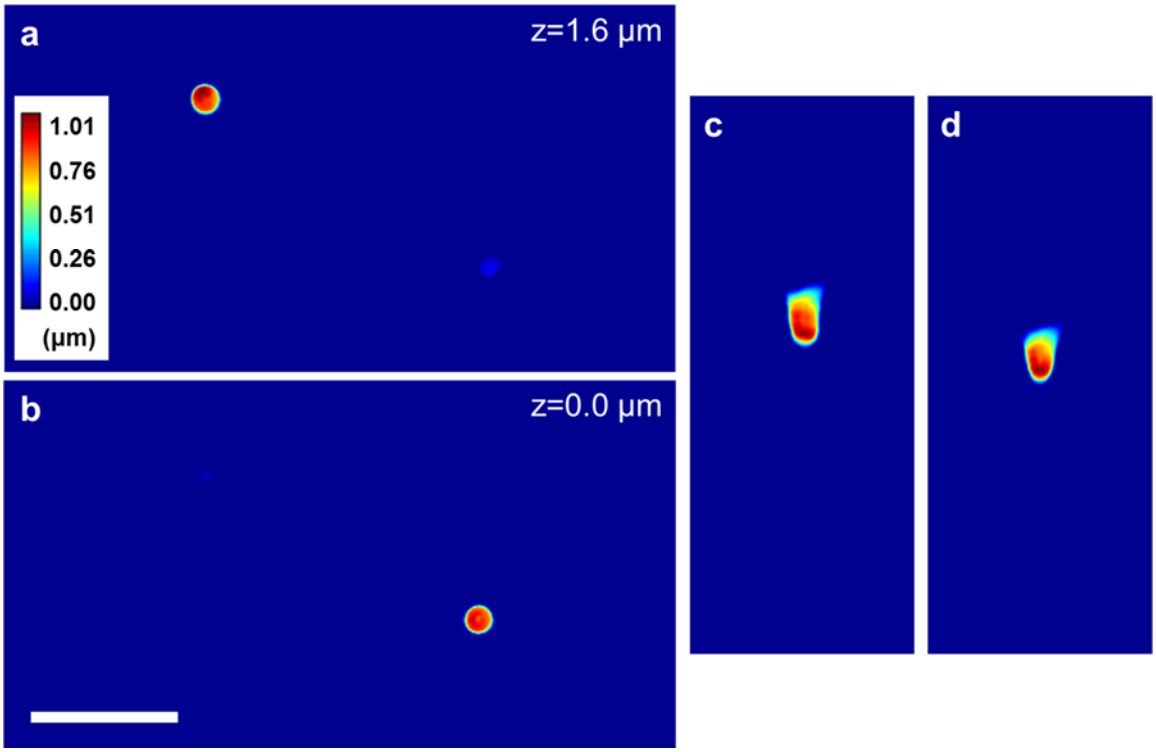

Figure S8. WDT tomogram of 1 μm polystyrene beads immersed in microscope objective immersion oil. (a) Quantitative height image at the focal position where the bead at top left corner of the field of view is in focus. The maximum height measured on the bead is 1.01 μm. (b) Quantitative height image at the focal position where the bead at the bottom right corner of the field of view is in focus. The maximum height measured on the bead is 0.95 μm. (c) Resliced image of the bead at the top left corner of (a). The longitudinal width of the bead is measured to be 1.32 μm and the transverse width is 0.97 μm. (d) Resliced image of the bead at the bottom right corner of (b). The longitudinal width of the bead is 1.27 μm and the transverse width is 0.94 μm. The scale bar indicates 5 μm in the sample plane.

i. Effect of dispersion introduced by a red blood cell

It is well known that hemoglobin (Hb) absorbs in the blue region of the visible spectrum. Here we investigate the effect on the WDT operation of this absorption and, thus, dispersion introduced by red blood cell (RBC) samples. From the refractive indices of H_2O[16], Hb[17], and human plasma[18, 19], the phase shift through an RBC with 2 μm thickness can be calculated as a function of radial frequency, ω. Using the molar extinction coefficient of Hemoglobin[20], the transmission amplitude through the cell can be calculated as well,. Figure S9 shows the phase shift, $\Delta\phi(\omega)$, and transmission amplitude, $|t(\omega)|$, for a RBC of typical thickness of 2 μm.

DOI: 10.1038/NPHOTON.2013.350

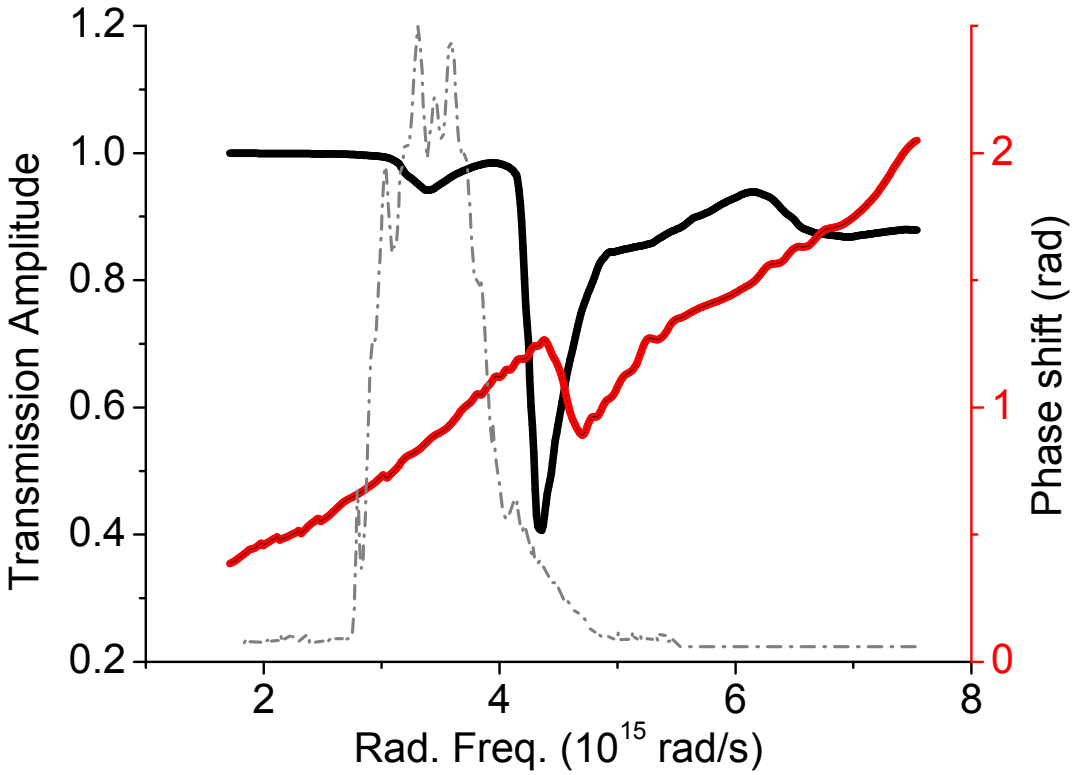

Figure S9. Transmission amplitude, $|t(\omega)|$, (black) and phase shift, $\Delta\phi(\omega)$, (red) through an RBC with 2 μm thickness. SLIM spectrum (gray) is overlaid to indicate the effective radial frequency range.

The complex transmission function through a RBC can then be represented as $t(\omega)=|t(\omega)|e^{i\Delta\varphi(\omega)}$. To quantitatively analyze the effects of $t(\omega)$ onto the PSF of WDT, we note that this function affects the cross-spectral density, W_{12}, via a multiplication operation, namely, $W_{12}'(\mathbf{k}_\perp,z,\omega)=t(\omega)W_{12}(\mathbf{k}_\perp,z,\omega)$. This procedure has been used for studying dispersion effects in low-coherence interferometry (see, e.g., Section 7.2. in Ref. [21]).

The cross-correlation function in Eq. (b14) becomes,

$$\begin{aligned}\Gamma_{12}(\mathbf{k}_\perp,z;0)&=\frac{1}{8\bar{n}^2}\int_0^\infty\frac{\left(Q^2+k_\perp^2\right)^2}{Q^3}S'\left(-\frac{Q^2+k_\perp^2}{2Q}\right)\chi(\mathbf{k}_\perp,Q)e^{izQ}dQ\\&=\frac{1}{8\bar{n}^2}FT_Q^{-1}\left[\frac{\left(Q^2+k_\perp^2\right)^2}{Q^3}S'\left(-\frac{Q^2+k_\perp^2}{2Q}\right)\right]\circledv_z\chi(\mathbf{k}_\perp,-z),\qquad\text{(i1)}\\&=\Sigma'(\mathbf{k}_\perp,-z)\circledv_z\chi(\mathbf{k}_\perp,-z)\end{aligned}$$

where $S'(\omega) = t(\omega)S(\omega)$. Taking the Fourier transform with respect to z, we obtain the modified version of Eq. (b15),

$$\Gamma_{12}(\mathbf{k}_\perp, Q; 0) = \Sigma'(\mathbf{k}_\perp, Q)\chi(\mathbf{k}_\perp, Q) \tag{i2}$$

where

$$\Sigma'(\mathbf{k}_\perp, Q) = \frac{1}{8\bar{n}^2}\frac{\left(Q^2 + k_\perp^2\right)^2}{Q^3} S'\left(-\frac{Q^2 + k_\perp^2}{2Q}\right) \tag{i3}$$

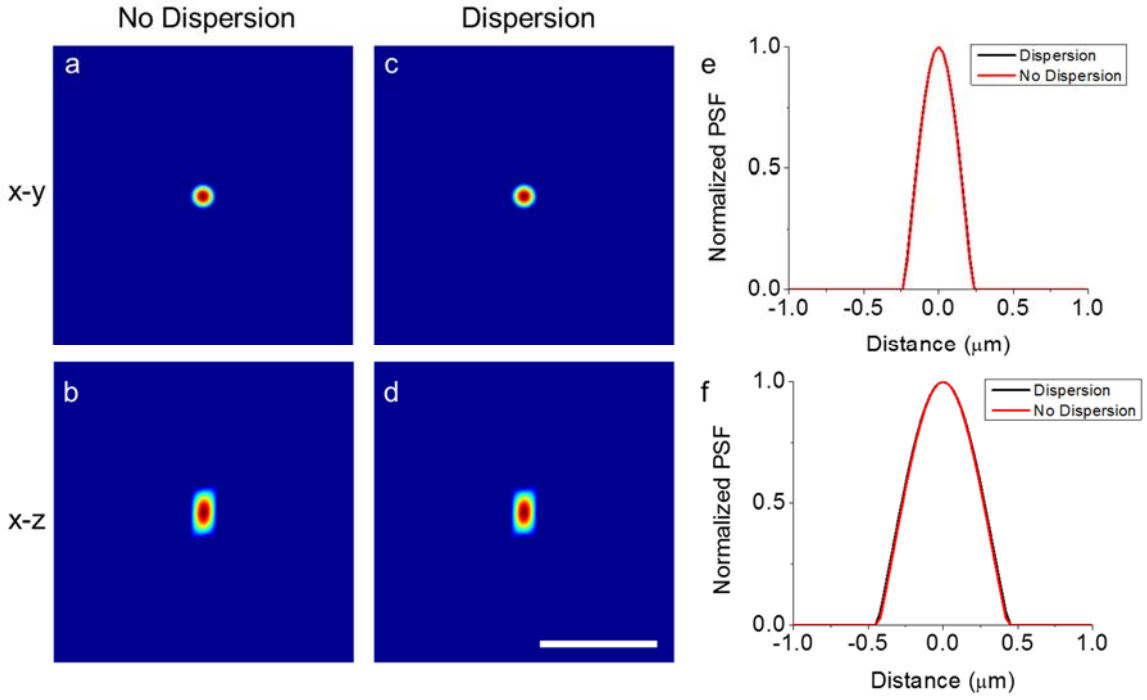

Figure S10. Comparison between the calculated PSF with and without dispersion. (a) and (b) Calculated PSF when there is no dispersion shown in the transverse and longitudinal direction, respectively. (c) and (d) the calculated PSF when there is dispersion effect on the sample shown in the transverse and longitudinal direction, respectively. (e) Horizontal profile through the center of the PSF in (a) and (c). (f) Vertical profile through the center of the PSF in (b) and (d). The scale bar corresponds to 2 μm.

Based on Eq. (i3), we compute the new PSF of the system, which now includes the effect of RBC dispersion and absorption. Figure S10 shows the cross-sections of calculated PSFs for the case without dispersion, S10a and S10b, and for the case with dispersion, S10c and S10d. To be consistent with the measurements, we applied threshold to the calculated PSF. Also, Fig. S10e and S10f show the transverse and longitudinal profiles through the center of the PSF, respectively.

The two PSFs are almost identical, with a very slight broadening caused by the dispersion. In the transverse dimension (Fig. S10e), the FWHM of the PSF with dispersion is 0.272 μm, while the FWHM of the case without dispersion is 0.268 μm. In the longitudinal dimension (Fig. S10f), the FWHM of the PSF with dispersion is 0.510 μm, while the FWHM of the case without

DOI: 10.1038/NPHOTON.2013.350

dispersion is 0.499 μm. Therefore, we can conclude that the dispersion and absorption in single red blood cells has a negligible effect on the overall performance of the WDT system.

This weak effect of dispersion through a RBC is expected. Since the illumination spectrum of the SLIM system only covers the radial frequency range roughly from 3.0×10^{15} rad/s to 4.0×10^{15} rad/s with considerable intensities, the effect of dispersion through an RBC can be limited to the same range as shown in Fig. S11. It can be seen that the transmission is fairly flat, while the spectral phase is essentially linear. Therefore, the transmission function of the RBC can be represented in the form of $t(\omega)=|t(\omega)|e^{i\alpha\omega}$ where $|t(\omega)|\approx1$ and $\alpha\omega$ is the linear phase shift. Since the linear phase shift does not change the shape of the cross-correlation function, but just shifts it in time. Therefore, we can conclude that the dispersion through a RBC has negligible effect on the entire imaging system.

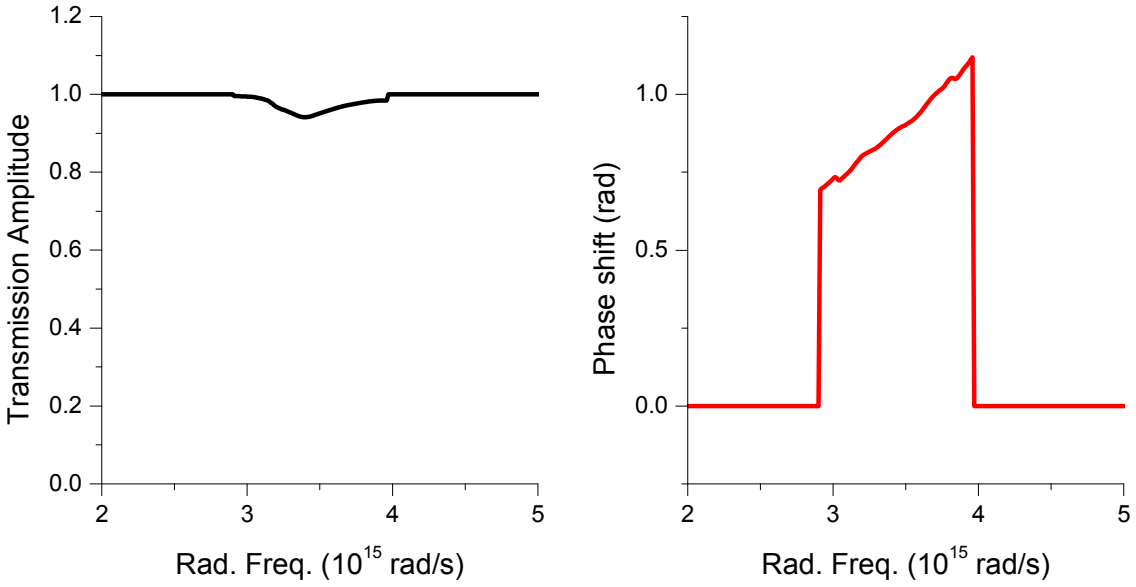

Figure S11. Transmission amplitude and phase shift through a 2 μm RBC in the SLIM spectrum window.

j. Point spread function vs. numerical aperture in WDT

Another method to assess the validity of WDT is to see the relationship between the resolution and the numerical aperture (NA). In order to do so, point spread function (PSF) for many different values of numerical aperture is calculated. Figure S12a shows the point spread functions in x-z plane, numerically calculated using WDT theory for various NA values ranging from 0.1 to 2. It is clear that for higher NA, the resolution is higher not only in the transverse dimension, but also in the longitudinal dimension. Figure S12b shows the linear relationship between the transverse resolution and inverse NA, and Fig. S12c shows the linear relationship between the longitudinal resolution and inverse NA squared. From this assessment, it is clear to say that WDT successfully model the light scattering.

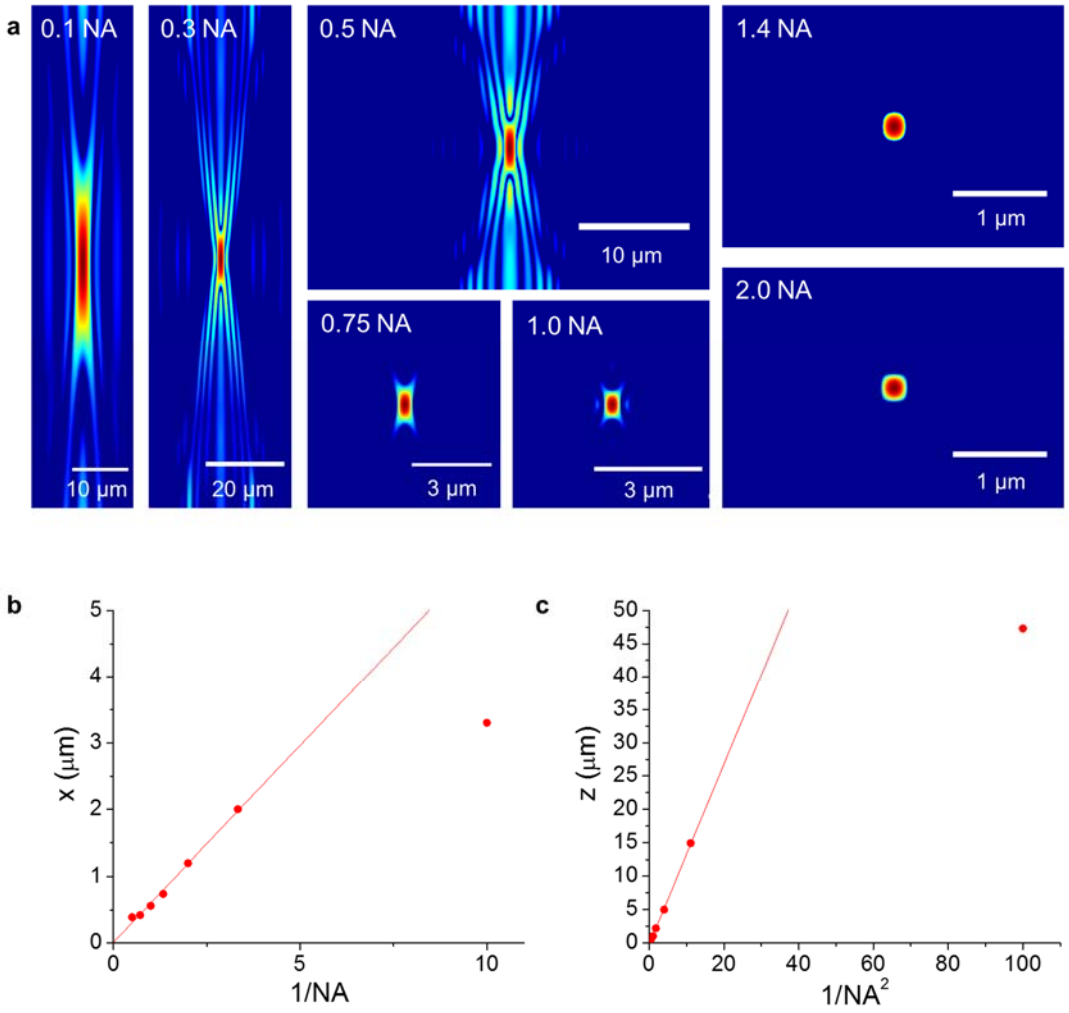

Figure S12. Point spread function calculated for various numerical aperture of the objective lens. (a) Point spread function for NA values ranging from 0.1 to 2, and shown in x-z plane. NA used for calculation and also the scale bars are indicated for each PSF separately. (b) Plot of transverse resolution as a function of inverse NA, where it clearly shows a well-defined linear relationship for most NA values. (c) Plot of longitudinal resolution as a function of inverse NA squared. It is clearly shown that the longitudinal is proportional to inverse NA squared.

DOI: 10.1038/NPHOTON.2013.350

References

1. Wang, Z., *et al.* Spatial light interference microscopy (SLIM). *Optics Express* **19**, 1016 (2011).
2. Wang, Z., *et al.* Topography and refractometry of nanostructures using spatial light interference microscopy. *Optics Letters* **35**, 208-210 (2010).
3. Mir, M., *et al.* Visualizing Escherichia coli Sub-Cellular Structure Using Sparse Deconvolution Spatial Light Interference Tomography. *PLoS ONE* **7**, e39816 (2012).
4. Mir, M., *et al.* Optical measurement of cycle-dependent cell growth. *Proceedings of the National Academy of Sciences* **108**, 13124-13129 (2011).
5. Wang, Z., *et al.* Label-free intracellular transport measured by Spatial Light Interference Microscopy. *J. Biomed. Opt.* **16**, 026019 (2011).
6. Wang, R., *et al.* Dispersion-relation phase spectroscopy of intracellular transport. *Optics Express* **19**, 20571-20579 (2011).
7. Mir, M., Tangella, K. & Popescu, G. Blood testing at the single cell level using quantitative phase and amplitude microscopy. *Biomedical optics express* **2**, 3259-3266 (2011).
8. Wang, Z., Popescu, G., Tangella, K.V. & Balla, A. Tissue refractive index as marker of disease (Journal Paper). *Journal of Biomedical Optics* **16**, 116017 (2011).
9. Sridharan, S., Mir, M. & Popescu, G. Simultaneous optical measurements of cell motility and growth. *Biomedical optics express* **2**, 2815-2820 (2011).
10. Wiener, N. Generalized harmonic analysis. *Acta Mathematica* **55**, 117-258 (1930).
11. Khintchine, A. Korrelationstheorie der stationären stochastischen Prozesse. *Mathematische Annalen* **109**, 604-615 (1934).
12. Donoho, D.L. For most large underdetermined systems of linear equations the minimal *Communications on pure and applied mathematics* **59**, 797-829 (2006).
13. Szameit, A., *et al.* Sparsity-based single-shot subwavelength coherent diffractive imaging. *Nature materials* (2012).
14. Shechtman, Y., Eldar, Y.C., Szameit, A. & Segev, M. Sparsity based sub-wavelength imaging with partially incoherent light via quadratic compressed sensing. *Optics Express* **19**, 14807-14822 (2011).
15. Babacan, S.D., Molina, R. & Katsaggelos, A.K. Sparse Bayesian image restoration. in *17th IEEE International Conference on Image Processing (ICIP)* 26-29 (2010).
16. Daimon, M. & Masumura, A. Measurement of the refractive index of distilled water from the near-infrared region to the ultraviolet region. *Applied Optics* **46**, 3811-3820 (2007).
17. Friebel, M. & Meinke, M. Model function to calculate the refractive index of native hemoglobin in the wavelength range of 250-1100 nm dependent on concentration. *Applied Optics* **45**, 2838-2842 (2006).
18. Vörös, J. The Density and Refractive Index of Adsorbing Protein Layers. *Biophysical journal* **87**, 553-561 (2004).
19. Adair, G.S. & Robinson, M.E. The specific refraction increments of serum-albumin and serum-globulin. *Biochemical Journal* **24**, 993 (1930).
20. Kim, T., Sridharan, S. & Popescu, G. Fourier Transform Light Scattering of Tissues. in *Handbook of Coherent-Domain Optical Methods* (ed. V.V. Tuchin) 259-290 (Springer, New York, 2013).
21. Popescu, G. *Quantitative phase imaging of cells and tissues* (McGraw Hill, 2011).